CrossMark

The NANOGrav 12.5-year Data Set: Search for Non-Einsteinian Polarization Modes in the Gravitational-wave Background

Zaven Arzoumanian[1], Paul T. Baker[2], Harsha Blumer[3,4], Bence Bécsy[5], Adam Brazier[6,7], Paul R. Brook[3,4],
Sarah Burke-Spolaor[3,4,8], Maria Charisi[9], Shami Chatterjee[6], Siyuan Chen[10,11,12], James M. Cordes[6], Neil J. Cornish[5],
Fronefield Crawford[13], H. Thankful Cromartie[6], Megan E. DeCesar[14,15,48], Dallas M. DeGan[16], Paul B. Demorest[17],
Timothy Dolch[18,19], Brendan Drachler[20,21], Justin A. Ellis[22], Elizabeth C. Ferrara[23,24,25], William Fiore[3,4],
Emmanuel Fonseca[26], Nathan Garver-Daniels[3,4], Peter A. Gentile[3,4], Deborah C. Good[27], Jeffrey S. Hazboun[28,48],
A. Miguel Holgado[29,30], Kristina Islo[31], Ross J. Jennings[6], Megan L. Jones[31], Andrew R. Kaiser[3,4], David L. Kaplan[31],
Luke Zoltan Kelley[32], Joey Shapiro Key[28], Nima Laal[16], Michael T. Lam[20,21], T. Joseph W. Lazio[33],
Duncan R. Lorimer[3,4], Tingting Liu[31], Jing Luo[34], Ryan S. Lynch[35], Dustin R. Madison[3,4,48], Alexander McEwen[31],
Maura A. McLaughlin[3,4], Chiara M. F. Mingarelli[36,37], Cherry Ng[38], David J. Nice[14], Ken D. Olum[39],
Timothy T. Pennucci[40,41,48], Nihan S. Pol[3,4,9], Scott M. Ransom[40], Paul S. Ray[42], Joseph D. Romano[43],
Shashwat C. Sardesai[31], Brent J. Shapiro-Albert[3,4], Xavier Siemens[16,31], Joseph Simon[33,44], Magdalena S. Siwek[45],
Renée Spiewak[46], Ingrid H. Stairs[27], Daniel R. Stinebring[47], Kevin Stovall[17], Jerry P. Sun[16], Joseph K. Swiggum[14,48],
Stephen R. Taylor[9], Jacob E. Turner[3,4], Michele Vallisneri[33], Sarah J. Vigeland[31], Haley M. Wahl[3,4], and
Caitlin A. Witt[3,4]
The NANOGrav Collaboration

[1] X-Ray Astrophysics Laboratory, NASA Goddard Space Flight Center, Code 662, Greenbelt, MD 20771, USA
[2] Department of Physics and Astronomy, Widener University, One University Place, Chester, PA 19013, USA
[3] Department of Physics and Astronomy, West Virginia University, P.O. Box 6315, Morgantown, WV 26506, USA
[4] Center for Gravitational Waves and Cosmology, West Virginia University, Chestnut Ridge Research Building, Morgantown, WV 26505, USA
[5] Department of Physics, Montana State University, Bozeman, MT 59717, USA
[6] Cornell Center for Astrophysics and Planetary Science and Department of Astronomy, Cornell University, Ithaca, NY 14853, USA
[7] Cornell Center for Advanced Computing, Cornell University, Ithaca, NY 14853, USA
[8] CIFAR Azrieli Global Scholars program, CIFAR, Toronto, Canada
[9] Department of Physics and Astronomy, Vanderbilt University, 2301 Vanderbilt Place, Nashville, TN 37235, USA
[10] Station de Radioastronomie de Nancay, Observatoire de Paris, Universite PSL, CNRS, Universite d'Orleans, F-18330 Nancay, France
[11] FEMTO-ST Institut de recherche, Department of Time and Frequency, UBFC and CNRS, ENSMM, F-25030 Besancon, France
[12] Laboratoire de Physique et Chimie de l'Environment et de l'Espace, LPC2E UMR7328, Universite d'Orleans, CNRS, F-45071 Orleans, France
[13] Department of Physics and Astronomy, Franklin & Marshall College, P.O. Box 3003, Lancaster, PA 17604, USA
[14] Department of Physics, Lafayette College, Easton, PA 18042, USA
[15] George Mason University, Fairfax, VA 22030, resident at U.S. Naval Research Laboratory, Washington, DC 20375, USA
[16] Department of Physics, Oregon State University, Corvallis, OR 97331, USA; laaln@oregonstate.edu
[17] National Radio Astronomy Observatory, 1003 Lopezville Road, Socorro, NM 87801, USA
[18] Department of Physics, Hillsdale College, 33 East College Street, Hillsdale, MI 49242, USA
[19] Eureka Scientific, Inc., 2452 Delmer Street, Suite 100, Oakland, CA 94602-3017, USA
[20] School of Physics and Astronomy, Rochester Institute of Technology, Rochester, NY 14623, USA
[21] Laboratory for Multiwavelength Astrophysics, Rochester Institute of Technology, Rochester, NY 14623, USA
[22] Infinia ML, 202 Rigsbee Avenue, Durham, NC 27701, USA
[23] Department of Astronomy, University of Maryland, College Park, MD 20742, USA
[24] Center for Research and Exploration in Space Science and Technology, NASA/GSFC, Greenbelt, MD 20771, USA
[25] NASA Goddard Space Flight Center, Greenbelt, MD 20771, USA
[26] Department of Physics, McGill University, 3600 University Street, Montreal, QC H3A 2T8, Canada
[27] Department of Physics and Astronomy, University of British Columbia, 6224 Agricultural Road, Vancouver, BC V6T 1Z1, Canada
[28] University of Washington Bothell, 18115 Campus Way NE, Bothell, WA 98011, USA
[29] Department of Astronomy and National Center for Supercomputing Applications, University of Illinois at Urbana-Champaign, Urbana, IL 61801, USA
[30] McWilliams Center for Cosmology and Department of Physics, Carnegie Mellon University, Pittsburgh, PA 15213, USA
[31] Center for Gravitation, Cosmology and Astrophysics, Department of Physics, University of Wisconsin–Milwaukee, P.O. Box 413, Milwaukee, WI 53201, USA
[32] Center for Interdisciplinary Exploration and Research in Astrophysics (CIERA), Northwestern University, Evanston, IL 60208, USA
[33] Jet Propulsion Laboratory, California Institute of Technology, 4800 Oak Grove Drive, Pasadena, CA 91109, USA
[34] Department of Astronomy & Astrophysics, University of Toronto, 50 St. George Street, Toronto, ON M5S 3H4, Canada
[35] Green Bank Observatory, P.O. Box 2, Green Bank, WV 24944, USA
[36] Center for Computational Astrophysics, Flatiron Institute, 162 5th Avenue, New York, NY 10010, USA
[37] Department of Physics, University of Connecticut, 196 Auditorium Road, U-3046, Storrs, CT 06269-3046, USA
[38] Dunlap Institute for Astronomy and Astrophysics, University of Toronto, 50 St. George Street, Toronto, ON M5S 3H4, Canada
[39] Tufts Institute of Cosmology, Department of Physics and Astronomy, Tufts University, 574 Boston Avenue, Medford, MA 02155, USA
[40] National Radio Astronomy Observatory, 520 Edgemont Road, Charlottesville, VA 22903, USA
[41] Institute of Physics, Eötvös Loránd University, Pázmány P.s. 1/A, 1117 Budapest, Hungary
[42] Space Science Division, Naval Research Laboratory, Washington, DC 20375-5352, USA
[43] Department of Physics and Astronomy, Texas Tech University, Lubbock, TX 79409-1051, USA
[44] Department of Astrophysical and Planetary Sciences, University of Colorado, Boulder, CO 80309, USA
[45] Center for Astrophysics, Harvard University, Cambridge, MA 02138, USA
[46] Centre for Astrophysics and Supercomputing, Swinburne University of Technology, P.O. Box 218, Hawthorn, VIC 3122, Australia

[47] Department of Physics and Astronomy, Oberlin College, Oberlin, OH 44074, USA

Abstract

We search NANOGrav's 12.5 yr data set for evidence of a gravitational-wave background (GWB) with all the spatial correlations allowed by general metric theories of gravity. We find no substantial evidence in favor of the existence of such correlations in our data. We find that scalar-transverse (ST) correlations yield signal-to-noise ratios and Bayes factors that are higher than quadrupolar (tensor-transverse, TT) correlations. Specifically, we find ST correlations with a signal-to-noise ratio of 2.8 that are preferred over TT correlations (Hellings and Downs correlations) with Bayesian odds of about 20:1. However, the significance of ST correlations is reduced dramatically when we include modeling of the solar system ephemeris systematics and/or remove pulsar J0030 +0451 entirely from consideration. Even taking the nominal signal-to-noise ratios at face value, analyses of simulated data sets show that such values are not extremely unlikely to be observed in cases where only the usual TT modes are present in the GWB. In the absence of a detection of any polarization mode of gravity, we place upper limits on their amplitudes for a spectral index of $\gamma = 5$ and a reference frequency of $f_{\mathrm{yr}} = 1 \, \mathrm{yr}^{-1}$. Among the upper limits for eight general families of metric theories of gravity, we find the values of $A_{\mathrm{TT}}^{95\%} = (9.7 \pm 0.4) \times 10^{-16}$ and $A_{\mathrm{ST}}^{95\%} = (1.4 \pm 0.03) \times 10^{-15}$ for the family of metric spacetime theories that contain both TT and ST modes.

Unified Astronomy Thesaurus concepts: Gravitational waves (678); Pulsars (1306); General relativity (641); Non-standard theories of gravity (1118); Pulsar timing method (1305)

1. Introduction

Pulsar timing experiments (Sazhin 1978; Detweiler 1979) allow us to explore the low-frequency ($\sim$1–100 nHz) part of the gravitational-wave (GW) spectrum. By measuring deviations from the expected arrival times of radio pulses from an array of millisecond pulsars, we can search for a variety of GW signals and their sources. The most promising sources in the nanohertz part of the GW spectrum are supermassive binary black holes (SMBHBs) that form via the mergers of massive galaxies. Orbiting SMBHBs produce a stochastic GW background (GWB; Lommen & Backer 2001; Jaffe & Backer 2003; Volonteri et al. 2003; Wyithe & Loeb 2003; Enoki et al. 2004; Sesana et al. 2008; McWilliams et al. 2012; Sesana 2013; Ravi et al. 2015; Rosado et al. 2015; Kelley et al. 2016; Sesana et al. 2016; Dvorkin & Barausse 2017; Kelley et al. 2017; Bonetti et al. 2018; Ryu et al. 2018), individual periodic signals or continuous waves (CWs; Sesana et al. 2009; Sesana & Vecchio 2010; Mingarelli et al. 2012; Roedig & Sesana 2012; Ravi et al. 2012, 2015; Rosado et al. 2015; Schutz & Ma 2016; Mingarelli et al. 2017; Kelley et al. 2018), and transient GW bursts (van Haasteren & Levin 2010; Cordes & Jenet 2012; Ravi et al. 2015; Madison et al. 2017; Islo et al. 2019; Bécsy & Cornish 2021). We expect to detect the GWB first, followed by detection of individual SMBHBs (Siemens et al. 2013; Rosado et al. 2015; Taylor et al. 2016; Mingarelli et al. 2017) that stand out above the GWB. Detection of GWs from SMBHBs will yield insights into galaxy mergers and evolution not possible through any other means. Other potential sources in the nanohertz band include cosmic strings (Damour & Vilenkin 2000, 2001; Berezinsky et al. 2004; Damour & Vilenkin 2005; Siemens et al. 2006, 2007; Ölmez et al. 2010; Sanidas et al. 2013; Blanco-Pillado et al. 2018; Chang & Cui 2021; Ghayour et al. 2021; Gorghetto et al. 2021; Wu et al. 2021a; Blanco-Pillado et al. 2021;

Lin 2021; Chiang & Lu 2021; Lazarides et al. 2021; Chakrabortty et al. 2021; Ellis & Lewicki 2021), phase transitions in the early universe (Witten 1984; Caprini et al. 2010; Addazi et al. 2021; Arzoumanian et al. 2021; Di Bari et al.2021; Borah et al. 2021; Nakai et al. 2021; Brandenburg et al. 2021; Neronov et al. 2021), and relic GWs from inflation (Starobinskiǐ 1979; Allen 1988; Lazarides et al. 2021; Ashoor-ioon et al. 2021; Yi & Zhu 2021; Li et al. 2021; Poletti 2021; Vagnozzi 2021; Sharma 2021), all of which would provide unique insights into high-energy and early-universe physics.

The North American Nanohertz Observatory for Gravitational Waves (NANOGrav) has been taking pulsar timing data since 2004 and currently monitors over 70 pulsars (Ransom et al. 2019). NANOGrav is one of several pulsar timing arrays (PTAs) around the world, which include the European PTA (Desvignes et al. 2016), the Parkes PTA (Kerr et al. 2020), the Indian PTA (Joshi et al. 2018), and the Chinese PTA (Lee 2016). Two additional telescope-centered pulsar timing programs that use the MeerKAT telescope in South Africa (Bailes et al. 2016) and the CHIME telescope in Canada (Ng 2017) are ongoing. These collaborations form the International Pulsar Timing Array (Perera et al. 2019). In recent years, PTAs have produced increasingly longer and more sensitive data sets, resulting in upper limits on the GWB that have continued to improve (van Haasteren et al. 2011; Demorest et al. 2013; Shannon et al. 2013; Lentati et al. 2015; Shannon et al. 2015; Arzoumanian et al. 2016; Verbiest et al. 2016; Arzoumanian et al. 2018). Very recently, NANOGrav detected a common red noise process in its 12.5 yr data set (Arzoumanian et al. 2020, hereafter referred to as NG12.5). This common process could be the first hint of a stochastic background of GWs, but unfortunately, the data were not sufficiently sensitive to show statistically significant evidence for quadrupolar correlations (Hellings & Downs 1983), the telltale sign of a GWB.

The PTAs provide an important test bed for theories of gravity (Yunes & Siemens 2013). By modifying Einstein's theory of general relativity, alternative theories of gravity are often invoked to explain the origin of cosmic acceleration, provide an alternative to dark matter, and reconcile quantum mechanics and gravity, some of the most profound challenges

---

[48] NANOGrav Physics Frontiers Center Postdoctoral Fellow.

facing fundamental physics today (Yunes & Siemens 2013). General relativity predicts the existence of GWs that travel at the speed of light, are transverse, and have two polarizations. Other theories of gravity generically predict the existence of GWs with different properties: additional polarization modes and modified dispersion relations. For instance, metric theories of gravity can have up to six possible GW polarization modes (Eardley et al. 1973c, 1973). The PTA searches for alternative polarization modes of gravity can therefore shed light on important foundational questions by exploring the different types of correlations that these additional modes produce.

LIGO and VIRGO have already made possible a number of GW tests of general relativity (Abbott et al. 2016a, 2016b, 2017a, 2017b, 2018a, 2018b, 2019a, 2019b, 2020a, 2020b, 2020c, 2021-a, 2021b). Until very recently (Chen et al. 2021a, 2021b; Wu et al. 2021b), PTA data had not been used to perform GW tests of gravity

due to the absence of a strong signal that can be attributed to GWs. However, as we mentioned, this situation has changed (see NG12.5 and Goncharov et al. 2021). Even though NANOGrav's 12.5 yr data set did not contain strong evidence for quadrupolar correlations, the detection of a common red noise process brings PTAs to a regime where the exploration of non-Einsteinian theories could prove to be fruitful.

Due to the nature of pulsar timing experiments, PTAs offer advantages over interferometers for detecting new polarizations or constraining the polarization content of GWs. For instance, each line of sight to a pulsar can be used to construct an independent projection of the various GW polarizations, and since PTAs typically observe tens of pulsars, linear combinations of the data can be formed to measure or constrain each of the six polarization modes many times over (Lee et al. 2008; Chamberlin & Siemens 2012; Yunes & Siemens 2013; Gair et al. 2015). Additionally, PTAs have an enhanced response to the longitudinal polarization modes (Chamberlin & Siemens 2012; Cornish et al. 2018; O'Beirne et al. 2019). Indeed, the constraint on the energy density of longitudinal modes inferred from recent NANOGrav data is about 3 orders of magnitude better than the constraint for the transverse modes (Cornish et al. 2018).

In this paper, we complement our work in NG12.5 by searching for evidence of non-Einsteinian polarization modes of gravity. We start our analyses by studying simulated PTA data sets similar to NANOGrav's 12.5 yr data set (Pol et al. 2021) and show that for current data sets (with tens of pulsars having observational baselines less than 15 yr and for typical amplitudes of the GWB signal of $\sim 2 \times 10^{-15}$), the correlations induced by transverse modes of GWs can be hard to distinguish from one another. These results are shown first to set our expectations for our analyses of the data set in hand, as well as future data sets.

We then report on the results of detection analyses on our 12.5 yr data set. We analyze the data assuming that the observed stochastic common red noise process across pulsars is due to various possible polarization modes of gravity valid in metric theories of gravity and perform a suite of Bayesian and frequentist searches on our data.

We find that a model with a phenomenological correlation pattern, the GW-like monopole,[49] is the most favored model

---

[49] The GW-like monopole is a phenomenological correlation pattern (introduced first in this paper) that we have found to be the most preferred among all other tested correlation patterns by our 12.5 yr data set. This correlation pattern follows the equation $\Gamma_{ab}^{\mathrm{mono}} = \frac{\delta_{ab}}{2} + \frac{1}{2}$, in which δ_{ab} is the Kronecker delta function, and a and b are two pulsars. Refer to Section 2.3.1 for more information.

(being preferred by an odds ratio of over 100 to 1 compared to a model without correlations), followed by a model with correlations induced entirely by the scalar-transverse (ST) mode of gravity (the breathing mode). The latter finding was first reported by Chen et al. (2021a), though we disagree with some aspects of their methodology and conclusions. Note that on theoretical grounds, we expect the presence of these types of correlations to be accompanied by the standard quadrupolar +- and ×-modes of general relativity; metric theories of gravity have at least the +- and ×-modes and possibly additional modes. In addition, our simulations show that at short observational baselines, for weak correlations, it is hard to distinguish between the different polarization modes; specifically, we show that when only the +- and ×-modes of general relativity are present, one can nevertheless, by chance, find evidence in favor of ST (breathing) modes. We also find that the significance of nonquadrupolar correlations is reduced significantly (the Bayes factor drops to about 20) when the pulsar J0030+0451 is removed from our analyses. This pulsar has a history of being problematic in detection searches (Hazboun et al. 2020b), and our results point to the possibility of noise-modeling issues involving this millisecond pulsar (MSP). We conclude that the apparent (and weak) presence of non-Einsteinian polarization modes of gravity is likely unphysical but worth following up in analyses of future data sets.

Finally, since we do not find statistically significant evidence in favor of any correlations, we place upper limits on the amplitudes of all possible subsets of polarization modes of gravity predicted by metric spacetime theories.

The structure of this paper is as follows. In Section 2, we summarize alternative theories of gravity in the context of pulsar timing experiments. We begin the section with a discussion of the most general form the polarization tensor of GWs can have in a general metric theory of gravity and show the effects these generalized GWs have on PTA data. In Section 3, we apply these results to a series of simulated data sets and NANOGrav's 12.5 yr data set. In Section 4, we present our conclusions.

2. Background

In this section, we review some of the concepts related to pulsar timing and GWs in general metric theories of gravity necessary to lay the foundations for the stochastic GWB detection pipeline. We begin with the form of the most general GW polarization tensor and discuss the signature of a GWB in PTA data. We then present a way to integrate pulsar timing and non-Einsteinian polarization modes of gravity into a single framework that we can use to search a PTA data set for the GWB.

2.1. Polarization Modes in Metric Theories of Gravity

In a general metric theory of gravity, GWs can have up to six independent polarization modes (Eardley et al. 1973). Using the notation of Newman and Penrose (Newman & Penrose 1962) and adapting a coordinate system in which the GW travels along the $+z$-axis, these modes can be written in terms of the electric components of the Riemann tensor through the following relations (Eardley et al. 1973; Will 1993):

$$\psi_2(u) \equiv -\frac{1}{6} R_{0303}, \qquad (1)$$

$$\psi_3(u) \equiv -\frac{1}{2}R_{0103} + \frac{1}{2}iR_{0203}, \qquad (2)$$

$$\psi_4(u) \equiv -R_{0101} + R_{0202} + 2iR_{0102}, \qquad (3)$$

$$\phi_{22}(u) \equiv -R_{0101} - R_{0202}, \qquad (4)$$

$$A_{\text{spatial}} = \begin{bmatrix} A_B + A_+ & A_\times & A_{V1} \\ A_\times & A_B - A_+ & A_{V2} \\ A_{V1} & A_{V2} & A_L \end{bmatrix}, \qquad (5)$$

where $u = t - z$ is the retarded time, and $\text{Re}(\psi_4) = A_+$, $\text{Im}(\psi_4) = A_\times$, $\phi_{22} = A_B$, $\text{Re}(\psi_3) = A_{V1}$, $\text{Im}(\psi_3) = A_{V2}$, and $\psi_2 = A_L$ are the plus, cross, breathing, x-vector, y-vector, and longitudinal polarization modes of gravity, respectively. This particular choice of the six independent components has the advantage of yielding the standard result of general relativity in the transverse-traceless gauge when all modes except cross and plus are set to zero:

$$A_{\text{spatial}}^E = \begin{bmatrix} A_+ & A_\times & 0 \\ A_\times & -A_+ & 0 \\ 0 & 0 & 0 \end{bmatrix}. \qquad (6)$$

Equation (5) is sufficient to search for all six polarization modes of gravity in pulsar timing data in a fully general way, i.e., without constraining ourselves to a particular metric theory of gravity.

2.2. Isotropic GWB and Pulsar Timing

The GWs perturb the geodesics of photons traveling from a pulsar to our radio telescopes on Earth. In the late 1970s, Sazhin (1978) and Detweiler (1979) first calculated this effect and expressed it in terms of the redshifting and blueshifting induced by a continuous GW propagating through the Earth–pulsar system. Setting the speed of light, as well as Newton's constant, to unity ($c = G = 1$), the GW-induced redshifts for the signals from pulsar a are of the form

$$z_a = \frac{\hat{n}_a^i \hat{n}_a^j}{2(1 + \hat{\Omega} \cdot \hat{n}_a)}[h_{ij}^e - h_{ij}^p], \qquad (7)$$

where $h_{ij}^e = h_{ij}(t, \vec{X} = 0)$ is the metric perturbation at the Earth when the pulse is received, $h_{ij}^p = h_{ij}(t - d_a, \vec{X} = d_a\hat{n}_a)$ is the metric perturbation at the pulsar when the pulse is emitted, $\hat{n}_a$ is a unit vector pointing from the Earth to the pulsar a, $\hat{\Omega}$ is a unit vector in the direction of propagation of the GW, and d_a is the distance to pulsar a. The terms proportional to h_{ij}^e and h_{ij}^p are usually referred to as the Earth and pulsar terms. The metric perturbation can be written in terms of a plane wave expansion as

$$h_{ij}(x^\mu) = \sum_A \int_{-\infty}^{\infty} df \int d\hat{\Omega}\, \tilde{h}_A(f, \hat{\Omega})\varepsilon_{ij}^A(\hat{\Omega})e^{-2\pi if(t - \vec{X}\cdot\hat{n})}, \qquad (8)$$

where A denotes the polarization mode, $\varepsilon_{ij}^A(\hat{\Omega})$ is the polarization tensor of the GW coming from the $\hat{\Omega}$ direction, and f is the frequency of GWs. Using this expansion, we can reexpress the total redshift induced by GWs in the form

$$z_a(t) = \sum_A \int_{-\infty}^{\infty} df \int d\hat{\Omega}\, \tilde{h}_A(f, \hat{\Omega})F_a^A(\hat{\Omega})e^{-2\pi ift}U_a(f, \hat{\Omega}), \qquad (9)$$

with

$$F_a^A(\hat{n}) = \frac{\hat{n}_a^i \hat{n}_a^j \varepsilon_{ij}^A(\hat{\Omega})}{2(1 + \hat{\Omega} \cdot \hat{n}_a)}, \qquad (10)$$

$$U_a(f, \hat{\Omega}) = [1 - e^{2\pi ifd_a(1 + \hat{\Omega}\cdot\hat{n}_a)}], \qquad (11)$$

where F_a^A are the so-called antenna pattern functions.

In pulsar timing, we measure the pulsar timing $R(t)$ residuals rather than the redshifts. The GW contribution to the residuals is simply the integral of the GW-induced redshifts, i.e,

$$R_a^{\text{GW}}(t) = \int_0^t dt'\, z_a(t'). \qquad (12)$$

Taking the stochastic GWB to be isotropic, unpolarized, and stationary, the correlation function for the strain can be written as

$$\langle \tilde{h}_A^*(f, \hat{\Omega})\tilde{h}_{A'}(f', \hat{\Omega}')\rangle = \delta(f - f')\frac{\delta^2(\hat{\Omega}, \hat{\Omega}')}{4\pi}\delta_{AA'}$$
$$\times \frac{1}{2}H(f), \qquad (13)$$

where $H(f)$ is the one-sided power spectral density of the GWB. This quantity is related to the fractional energy density spectrum in GWs, $\Omega_{\text{GW}}(f)$, through the equation

$$H(f) = \frac{3H_0^2}{2\pi^2}\frac{\Omega_{\text{GW}}(f)}{f^3}, \qquad (14)$$

where H_0 is the present value of the Hubble parameter, and

$$\Omega_{\text{GW}}(f) = \frac{1}{\rho_c}\frac{d\rho_{\text{GW}}}{d\ln(f)} \qquad (15)$$

for critical density ρ_c and GW energy density ρ_{GW}. Combining Equations (9), (12), and (13) results in

$$\langle R_a^{\text{GW}} R_b^{\text{GW}}\rangle = \sum_A \int_{f_L}^{f_H} df \frac{H(f)}{(2\pi f)^2}\text{Re}\,\{\Gamma_{ab}^A(\xi_{ab}, f)\} \qquad (16)$$

for

$$\Gamma_{ab}^A(\xi_{ab}, f) = \int_0^{2\pi} d\phi \int_0^\pi d\theta \gamma_{ab}^A$$
$$\gamma_{ab}^A = \sin(\theta) U_a(f, \Omega) U_b^*(f, \Omega) F_a^A(\hat{n}) F_b^A(\hat{n}), \qquad (17)$$

where f_H and f_L are the upper and lower bounds of frequency, and Γ_{ab}^A is the so-called overlap reduction function (ORF). The ORF is a function of the angular separation ξ_{ab} between two pulsars and the GW frequency f. This function plays a key role in GW stochastic background searches in a PTA data set.

2.3. Explicit Form of the GWB Signal in a PTA Data Set

Here we discuss (i) the properties of the ORFs for each of the polarization modes and (ii) the characterization of the power spectral density of GWs. These provide the final set of tools for creating the framework that enables us to search our 12.5 yr
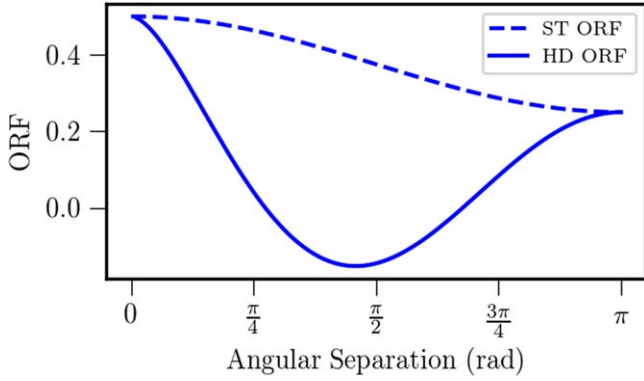
Figure 1. The ORFs ($a \neq b$) for the transverse polarization modes of gravity normalized to $1/2$ at zero angular separation. The solid line is the TT mode ORF, and the dashed line is the ST-mode ORF.

data set for evidence of the existence of non-Einsteinian polarization modes of gravity.

2.3.1. Overlap Reduction Functions

The ORFs for all polarization modes of gravity have been studied extensively in the literature (see, e.g., Chamberlin & Siemens 2012 and Gair et al. 2015). In the following, we summarize the most important results of these studies.

For the tensor-transverse (TT) mode of gravity, the ORF is found to be

$$\Gamma_{ab}^{TT} = \Gamma_{ab}^{\times} + \Gamma_{ab}^{+} \simeq \frac{\delta_{ab}}{2} + C(\xi_{ab}), \qquad (18)$$

where δ_{ab} is the Kronecker delta function and $C(\xi_{ab})$ is best known as the Hellings and Downs (HD) correlations (Hellings & Downs 1983),

$$C(\xi_{ab}) = \frac{3}{2}\left\{\frac{1}{3} + k_{ab}\left[\ln(k_{ab}) - \frac{1}{6}\right]\right\}, \qquad (19)$$

for

$$k_{ab} = \frac{1 - \cos(\xi_{ab})}{2}. \qquad (20)$$

To an excellent approximation, the HD correlation curve is frequency- and pulsar distance–independent for all angular separations over the range of fd_a values relevant to pulsar timing experiments (Anholm et al. 2009). This can be understood by noting that the ratio of pulsar distances to the GW wavelengths at nanohertz frequencies is large (typically larger than 100); hence, the exponential terms of Equation (17) oscillate rapidly while making a negligible contribution to the overall integral. Additionally, in the case of $\xi_{aa} = 0$ (i.e., $a = b$), the product of $U_a(f, \hat{\Omega})$ and $U_a^*(f, \hat{\Omega})$ doubles the value of the ORF relative to what $C(\xi_{ab})$ gives alone, hence the need for δ_{ab} in Equation (18).

For the ST mode, also known in the literature as the breathing mode, the ORF is found to be (Chamberlin & Siemens 2012)

$$\Gamma_{ab}^{ST} \approx \frac{\delta_{ab}}{2} + \frac{1}{8}(3 + \cos(\xi_{ab})). \qquad (21)$$

Similar to the case of the TT modes, the ST-mode ORF is frequency- and pulsar distance–independent to an excellent approximation. Figure 1 shows the transverse ORFs as a function of angular separation for the case of $a \neq b$.

Figure 2. The ORF for the VL polarization modes of gravity. Here we have taken $a \neq b$. Note that the values on the y-axis at low angular separations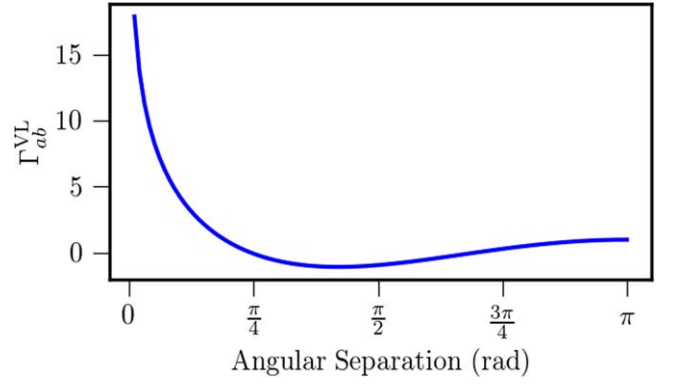 are significantly larger than for the TT and ST modes (see Figure 1). The PTAs are more sensitive to VL modes than transverse modes.

For the vector longitudinal (VL) modes, the ORF is found to be (Lee et al. 2008)

$$\Gamma_{ab}^{VL} = \Gamma_{ab}^{(VL)_y} + \Gamma_{ab}^{(VL)_x}$$

$$\approx 3\log\left(\frac{2}{1 - \cos(\xi_{ab})}\right) - 4\cos(\xi_{ab}) - 3, \qquad (22)$$

where a normalization factor of $3/(4\pi)$ has been applied for consistency with the transverse ORFs (see Figure 2) and $a \neq b$. These modes are also frequency independent in the limit of large fd_a values relevant to pulsar timing, albeit to a lesser extent than the transverse modes. The approximation fails at zero angular separations requiring the inclusion of the pulsar (exponential) terms in the calculation of ORF to cancel the divergence. For the case of $a = b$ (i.e., the case of a pulsar correlated with itself), Γ_{aa}^{VL} is (Lee et al. 2008)

$$\Gamma_{aa}^{VL} = 6\ln(4\pi d_a f) - 14 + 6\gamma_E, \qquad (23)$$

where γ_E is Euler's constant, and $fd_a \gg 1$.

Finally, for the scalar longitudinal (SL) mode, the ORF cannot be evaluated analytically for all angular separations. Hence, the integral in Equation (17) needs to be evaluated numerically given a set of pulsar distances, frequencies, and angular separations. Figure 3 shows the strong dependence of Γ_{ab}^{SL} to fd_a values. However, similar to the case of VL modes, for the case of $a = b$ and large fd_a values, an estimate of Γ_{aa}^{SL} can be found (Chamberlin & Siemens 2012):

$$\Gamma_{aa}^{SL} = \frac{3\pi^2}{4}fd_a - 3\ln(4\pi fd_a) + \frac{37}{8} - 3\gamma_E. \qquad (24)$$

So far, we have only discussed ORFs that result from generic metric theories of gravity. In light of the results presented in NG12.5, namely, a high signal-to-noise ratio (S/N) estimate for a monopolar process, it will be useful to define other ORFs that are more phenomenological in nature and not necessarily due to any single metric theory of gravity. Two such ORFs are the GW-like monopole and GW-like dipole, with the explicit forms

$$\Gamma_{ab}^{GW-mono} = \frac{\delta_{ab}}{2} + \frac{1}{2}, \qquad (25)$$

$$\Gamma_{ab}^{GW-dipole} = \frac{\delta_{ab}}{2} + \frac{\cos\xi_{ab}}{2}. \qquad (26)$$
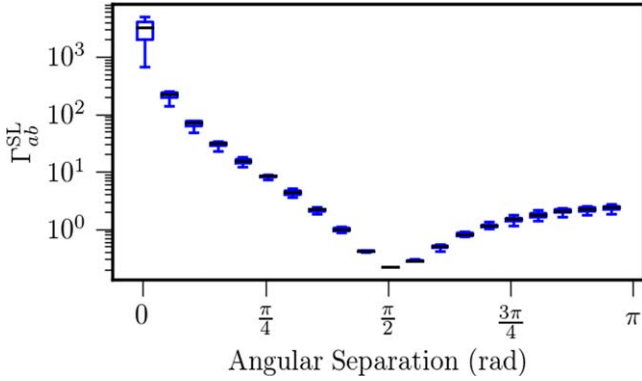
Figure 3. Box plots for the ORF for the SL mode of gravity. The box plots depict the variance of the SL ORF over fd_a values ranging from 100 to 1000. Pulsars a and b are assumed to be different. Note the much larger values on the y-axis compared to the transverse (Figure 1) and VL (Figure 2) modes showing that the SL mode will produce the largest signal in a PTA.

We will use these ORFs when searching NANOGrav's 12.5 yr data set and compare them to the different polarization modes of gravity, specifically the results of ST-mode searches. These ORFs should not be confused with systematic monopole (e.g., clock error–induced) or dipole (e.g., ephemeride-induced) uncertainties, as those produce correlations that do not distinguish between coaligned pulsars (i.e., $\Gamma(\xi_{ab} = 0)$) and a pulsar paired with itself (i.e., $\Gamma(\xi_{aa} = 0)$). Namely, the types of correlations in Equations (25) and (26) only affect half of the signal, the Earth term, whereas clock and ephemeride errors affect the entire signal. This is the reason we introduce the terminology *GW-like* to these phenomenological ORFs.

It is worth noting that even though a pure monopole of the form of Equation (25) is not predicted by any metric theory of gravity, massive GWs originating from a scalar–tensor metric theory of gravity could alter the form of the ST ORF into more of a monopolar-looking correlation pattern (Qin et al. 2021). For example, a metric theory of gravity can have two types of contributions to the GWB, a massive ST-wave contribution of the form

$$\sigma_{ij}(x^\mu) = \int_{-\infty}^{\infty} df \int d\hat{\Omega} \tilde{\sigma}(f, \hat{\Omega}) \varepsilon_{ij}^{ST}(\hat{\Omega}) e^{Y_\sigma(f,m)}, \qquad (27)$$

$$Y_\sigma(f, m) = -2\pi i f \left(t - d \sqrt{1 - \frac{m^2}{4\pi^2 f^2}} \right) \qquad (28)$$

and a massless transverse tensor contribution of the form

$$h_{ij}(x^\mu) = \int_{-\infty}^{\infty} df \int d\hat{\Omega} \tilde{h}_{TT}(f, \hat{\Omega}) \varepsilon_{ij}^{TT}(\hat{\Omega}) e^{Y_h}, \qquad (29)$$

$$Y_h = -2\pi i f (t - d), \qquad (30)$$

where d is the distance to a pulsar. Depending on the values of the mass and frequency, the resulting ORF due to the ST mode could approach a monopolar form (see Qin et al. 2021 for a detailed discussion).

2.3.2. Spectral Density of GWs and Correlations in Timing Residuals

In PTA analyses, the spectral density H is often written in terms of the dimensionless characteristic strain h_c, defined by

$$h_c(f) \equiv \sqrt{fH(f)}. \qquad (31)$$

NANOGrav analyses have included various models for the characterization of h_c, including a power-law model, free-spectral model, and broken power-law model, depending on the nature of the analysis (see, e.g., the 12.5 yr GWB analysis; Arzoumanian et al. 2020). In this paper, we will restrict ourselves to the power-law model.

For each polarization mode of gravity, we will use

$$h_c(f) = A \left(\frac{f}{f_{yr}} \right)^\alpha, \qquad (32)$$

where A is a dimensionless amplitude, f_{yr} is a reference frequency chosen to be $1/1(yr)$, and α is the spectral index. The values of the amplitude and spectral index depend on the sources that produce the GWs and the polarization content of the metric theory under consideration. The expected correlation in the timing residual time series for two pulsars can be written as follows:

$$\langle R_a R_b \rangle = \int_{f_L}^{f_H} df S_{ab}(f), \qquad (33)$$

where

$$S_{ab} = \sum_m \Gamma_{ab}^m A_m^2 \left(\frac{f}{f_{yr}} \right)^{3-\gamma_m} \frac{1}{8\pi^2 f^3} \qquad (34)$$

for the sum ranging over all six polarization modes and

$$\gamma_m \equiv 3 - 2\alpha_m. \qquad (35)$$

Hereafter, the term *spectral index* will refer to the value of γ_m rather than α_m.

3. Searches for Non-Einsteinian Modes in the GWB

Real pulsar timing data sets require significantly more complex modeling than what Equation (34) might suggest. Equation (34) only includes the GWB content of the pulsar timing residuals; other chromatic (radio frequency–dependent) and achromatic noise contributions to the timing residuals need to be included in a robust detection analysis. Furthermore, astrophysical processes such as stellar scattering and dipole radiation of binary sources of GWs would complicate the picture even further (see Appendix A for a discussion of dipole radiation). To accomplish this goal, we add the stochastic GW signal modeling presented here to our already-existing detection pipeline and pulsar inference tool, ENTERPRISE (Ellis et al. 2020), and search for various polarization modes of gravity using NANOGrav's 12.5 yr data set.

The detection procedure for the ST and VL modes does not require significant modifications to the already-existing tools for searches for isotropic GWBs in ENTERPRISE. This is due to the fact that the cross-correlation curves are a function of angular separation only, and not frequency. However, the similarities between some of the tensorial ORFs, such as the GW-like dipole, GW-like monopole, HD, and ST correlations, can pose a significant detection challenge; distinguishing between these ORFs requires high-significance measurements of the cross-correlated power as a function of the angular separation. Figure 4 shows the ORFs for the TT and ST modes, as well as the GW-like monopole and dipole. It is easy to see that given large enough uncertainties in the cross-correlations,
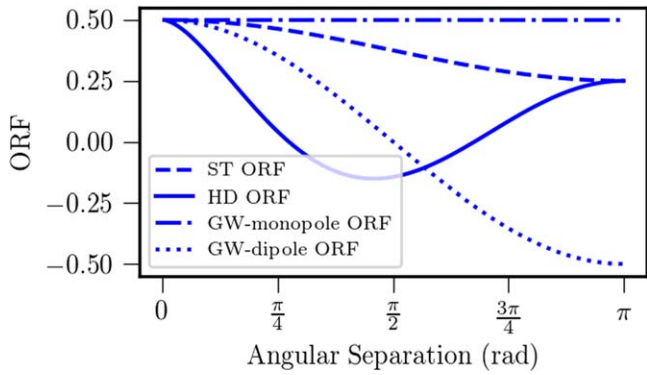
Figure 4. The solid line is the HD correlation curve, the dashed line is the ST ORF, the dashed–dotted line is the GW-monopole ORF, and the dotted line is the GW-dipole ORF. These four ORFs can be hard to distinguish if the uncertainties in the timing residual cross-correlations are sufficiently large.

the detection of a data set's actual correlation pattern can become problematic.

To address the challenge of reduction of the uncertainties of the cross-correlations, improvements in four key areas can be pursued: (i) increasing the observation time, (ii) improving the observing instrumentation used at our radio telescopes, (iii) increasing the number of pulsars being observed, and (iv) improving noise modeling of individual pulsars. All of these avenues are actively being pursued by NANOGrav.

In this section, we will use our detection pipeline to search for and set upper limits on the polarization modes present in general metric theories of gravity. We start by performing our analyses on simulated data sets and then proceed to perform similar analyses on NANOGrav's 12.5 yr data set. In this paper, we only perform upper limit analyses (not detection analyses; see Section 3.3) for the VL and SL polarization modes of gravity. This is for three reasons: (i) the large correlations at small angular separations predicted for the longitudinal (VL, SL) polarization modes are absent in the current data set; (ii) as shown in Figure 3, the values of the ORF for the SL mode are very sensitive to pulsar distances, which are not well known; and (iii) the addition of frequency-dependent terms to our current detection pipeline required for the SL mode demands significant modifications, testing, and simulations that are outside the scope of this work.

Although the required additions to our detection pipeline are currently under development and will be deployed in analyses of future data sets, we do not see the additions as necessary for the data set in hand, as the reasons denoted above by (i) and (ii) are among the current limitations of pulsar timing challenging the robustness of any detection search for the longitudinal polarization modes of gravity using pulsar timing data.

3.1. Detection of Additional Polarization Modes of Gravity in Simulated Pulsar Timing Data

It is useful to test our detection techniques on simulated data sets in order to set our expectations for the analysis presented in this paper and future projects.

The first simulated PTA data set we have analyzed is obtained from NANOGrav's Astro4cast project (Pol et al. 2021). The data set is made out of simulated pulsar times of arrival (TOAs) for the same 45 pulsars as used in NG12.5, with similar noise characteristics as are present in our real data set along with an injected GWB signal of amplitude $A_{TT} = 2 \times 10^{-15}$ and spectral
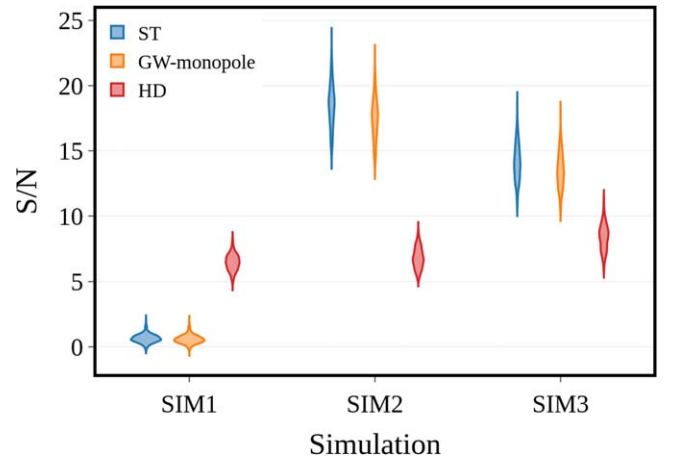
Figure 5. Violin plots depicting the S/N distribution of the noise-marginalized optimal statistic for one realization of simulated data sets SIM1, SIM2, and SIM3 (see the main text for a description). The data are searched for three different correlation patterns: ST (blue), HD (red), and GW-like monopole (orange). The S/N distribution for each simulated data set is obtained from the calculation of the noise-marginalized optimal statistic evaluated 1000 times. Even in the case of a strong injection of ST correlations (SIM2), GW-like monopole and ST correlations yield similar S/Ns.

index $\gamma = 13/3$. The observational baseline for this simulated data set is 20 yr. Hereon, we refer to this data set as SIM1.

The second (SIM2) and third (SIM3) simulated data sets are identical to SIM1 except for the polarization-mode content and the spectral indices of the injected GW signals. SIM2 has a GWB of ST GWs with $A_{ST} = 2 \times 10^{-15}$ and $\gamma_{ST} = 5$, and SIM3 has both ST- and TT-type GWBs with amplitudes of $A_{ST} = A_{TT} = 2 \times 10^{-15}$ and spectral indices of $\gamma_{ST} = 5$ and $\gamma_{TT} = 13/3$, respectively. All of the simulated data sets have been analyzed using NANOGrav's ENTERPRISE to search for a common correlated red noise process.

One of the most powerful and computationally inexpensive analyses is the noise-marginalized optimal statistic technique (Vigeland et al. 2018). Figure 5 shows the distributions for S/Ns of the optimal statistic with HD, monopole, and ST correlations and all three simulated data sets. We conclude the following as a result of these S/N calculations.

1. The high value of the S/N of the HD correlations relative to the monopole and ST correlations observed in SIM1 at late observational times gives us confidence that if significant HD correlations are present in our data, our current techniques are capable of detection without mistaking HD correlations for ST or GW-like monopole correlations.

2. The large value of the S/N of the TT mode observed in SIM2 suggests that an ST GWB signal could be mistaken for a TT GWB signal if the ST mode is excluded from a noise-marginalized optimal statistical analysis. Given that the optimal statistical and Bayesian analyses used by NG12.5 yield consistent results, ST-mode and monopolar correlations of Equation (25) need to be included in searches for a GWB signal to ensure an unbiased determination of the types of correlations present in a particular data set.

3. The ST and GW-like monopolar correlations yield broadly similar S/Ns. In fact, in the absence of an ST mode (as in SIM1), the two correlations give nearly identical S/Ns. Thus, distinguishing ST correlations from GW-like monopole correlations is challenging. See Appendix B for a brief discussion of one technique to distinguish ST from GW-like monopole correlations using the noise-marginalized optimal static.
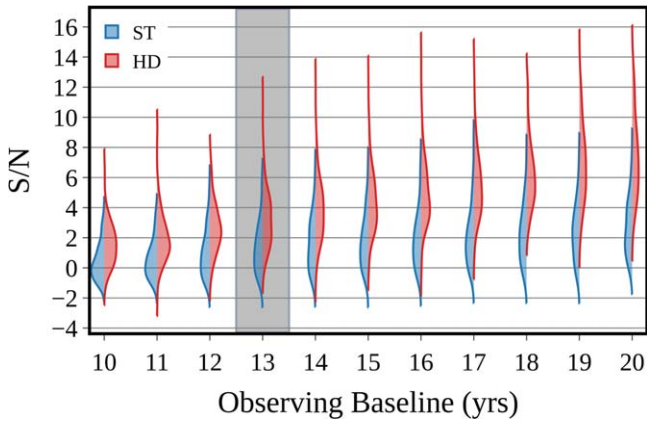
Figure 6. The S/N evolution for the optimal statistic using the SIM1 data set as a function of observation time. The split violin plots show the distribution of S/N over 100 different realizations of SIM1 for observing baselines of 10–20 yr for HD (red) and ST (blue) correlations. To obtain the S/N value for each realization, the noise-marginalized optimal statistic is performed 1000 times, and the median of the calculated S/Ns is plotted as the given S/N of that realization. The shaded region highlights the approximate region in which NANOGrav's 12.5 yr data sets reside, which is a regime where the correlated signal is weak and the correlations cannot be easily distinguished from one other. As the baseline increases, the distinction between the HD and ST S/N becomes more manifest. Specifically, 11% of realizations yield a higher S/N for ST than HD correlations at 13 yr, whereas 4% of realizations yield a higher S/N for ST than HD correlations at 20 yr. See the description of Figure 7.

To conclude this subsection, we discuss the evolution of the distributions for the S/N in SIM1 as a function of observational baseline, shown in Figures 6 and 7. One hundred different realizations of 10–20 yr slices of SIM1 are treated as independent data sets in which we find the S/N for HD and ST correlations (GW-like monopolar correlations are almost identical to ST correlations and hence are not shown) through the noise-marginalized optimal statistic technique. Each slice of SIM1 has 100 different realizations, making the total number of data sets 1100. These results confirm our earlier expectation for the degeneracy of ST and HD correlations (and GW-like monopole correlations) at short observational baselines. If a GWB signal with HD correlations is weak (in the case of SIM1, "weak" can be defined as having an amplitude of $A_{TT} = 2 \times 10^{-15}$ and a baseline of less than 15 yr), a GWB with HD correlations can be easily mistaken for an ST and GW-like monopolar GWB. This is due to the stochastic nature of the GWB and the nonisotropic sky distribution of pulsars used in the analyses. As can be seen in Figure 6, there is a significant overlap between S/Ns calculated for ST and TT modes, suggesting that we should not be surprised to observe a high relative S/N value of an ST or a GW-like monopole over the TT mode when only HD correlations are present but weak.

3.2. Searching for Non-Einsteinian Polarization Modes of Gravity in NANOGrav's 12.5 yr Data Set

The NANOGrav 12.5 yr data set was searched for an isotropic GWB consistent with Einstein's gravity in NG12.5. In this subsection, we extend the analyses presented in NG12.5 by including searches for common red noise processes with ST, HD, and GW-like monopole correlations and their expected spectral indices. A few issues are worth keeping in mind while interpreting the results of our searches.

1. When the correlations are weak, the transverse polarization modes of gravity can be easily mistaken for one another, as

seen in the S/N evolution analysis of SIM1. It is possible to obtain S/Ns as high as 3 for the ST (or GW-like monopole) mode, even in the case of the absence of such a mode in a PTA data set, so long as the TT mode is present.

2. Though a large optimal statistic S/N value for a particular mode of gravity can be significant, the amplitude of that mode as seen in the correlations needs to be consistent with the amplitude of the common red noise process. For instance, in NG12.5, we showed that a process with monopolar cross-correlations has an S/N distribution with a peak around 2.8 for a spectral index of $\gamma = 13/3$. However, the amplitude of this monopolar process was shown to be significantly smaller than the amplitude of the uncorrelated common red noise process, indicating that the majority of the common signal did not have monopolar correlations. This is because the optimal statistic estimate of the amplitude does not include the autocorrelation terms in the covariance matrix, only the cross-correlation terms. We show further examples of this below. In NG12.5, a monopolar process was disfavored in the full Bayesian analysis, which includes both auto- and cross-terms of the covariance matrix, due to the inconsistency of the amplitude of the common process with the best-fit cross-correlation-based estimate of the monopole amplitude.

3. The threshold for detection has to be large enough that it is robust to the modeling of uncertainties in the solar system ephemeris, BayesEphem (Vallisneri et al. 2020). Long term, this will not be a problem for detection of the TT mode; the impact of BayesEphem has been shown to be minimal as the observation time increases (see Vallisneri et al. 2020). This is likely true for the other modes, but the impact of BayesEphem on other polarization modes has not been fully explored to date.

4. Bayes factors, S/Ns, and upper limits are all model-dependent. Extreme care must be taken when interpreting Bayes factors, S/N values, or upper limit estimates; different choices for spectral indices, priors, and competing models can significantly affect the results of these calculations.

3.2.1. Bayesian Analyses

Before describing the results of the rest of the Bayesian analyses, it is worth defining our Bayesian modeling terminology clearly. Following the naming convention of NG12.5, two general types of Bayesian models have been used in this paper: M2A and M3A. Model M2A includes a common red noise process and pulsar intrinsic red noises, plus various back end–dependent white noise terms such as EFAC, ECORR, and EQUAD.[50] Model M2A does not include correlations between pulsars, so the full PTA covariance matrix is block-diagonal. Model M3A includes the same noise processes as M2A, with the addition of correlations of the common red noise process; i.e., the off-diagonal terms in the full PTA covariance matrix are populated. The types of correlations considered for an M3A model are specified in square brackets preceding the term "M3A." Furthermore, for both M2A and M3A, the choice of the spectral index of the common process is specified inside square brackets following "M2A" or "M3A." For example, [HD]M3A[5]

---

[50] The white noise components are EQUAD, which adds white noise in quadrature; ECORR, which describes white noise that is correlated within the same observing epoch but uncorrelated between different observing epochs; and EFAC, which scales the total template fitting TOA uncertainty after the inclusion of the previous two white noise terms. For all of these components, we used separate parameters for every combination of pulsar, back end, and receiver.
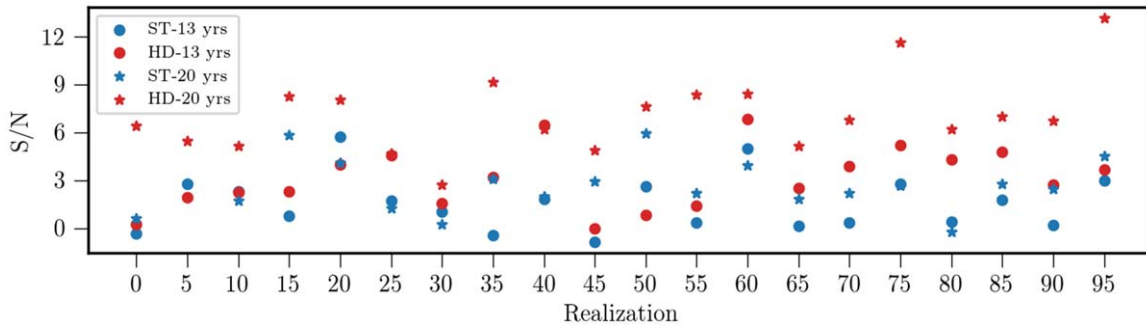
Figure 7. The S/N estimation using the noise-marginalized optimal statistic technique for 100 different realizations of SIM1 at observation baselines of 13 (circles) and 20 (stars) yr. For clarity, only 20 realizations out of 100 are shown. In blue, we show the S/N values of ST, and in red, we show the S/N values of HD correlations. Over the 100 realizations, 11 yield a higher S/N for ST than HD correlations at 13 yr, whereas four out of 100 yield a higher S/N for ST than HD correlations at 20 yr.
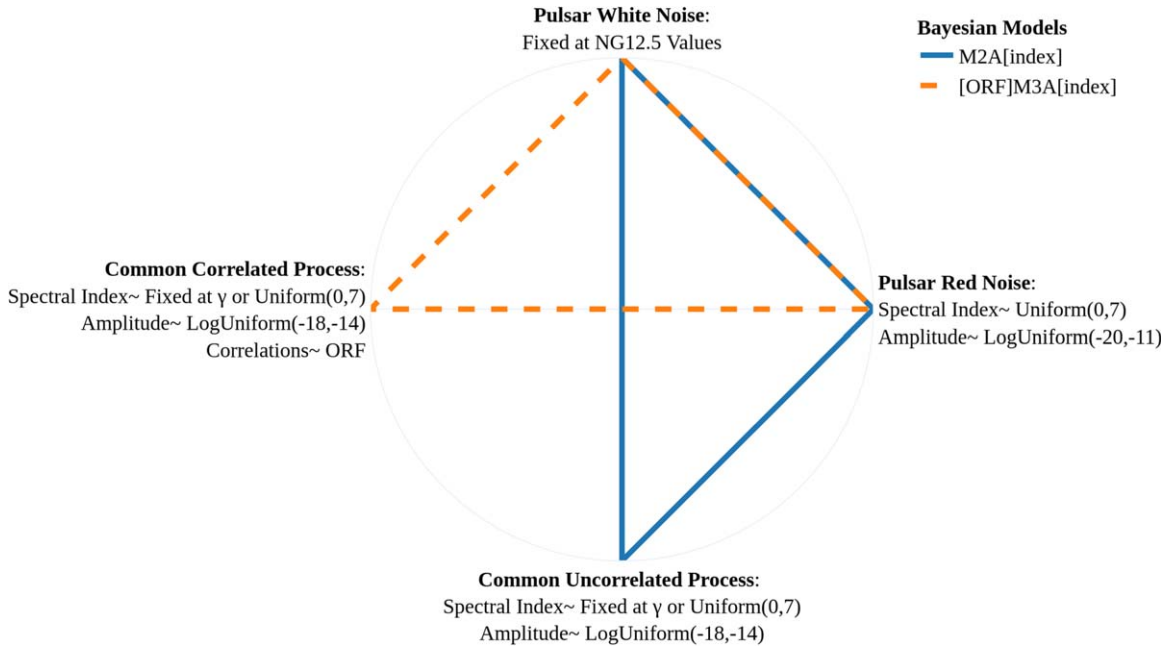
Figure 8. Chart depicting the structure of the Bayesian models used. The blue solid line connects the pieces of an M2A[index] model, while the orange dashed line connects the pieces of an [ORF]M3A[index] model. As can be seen from the figure, an M2A model consists of pulsar intrinsic red noise, white noise, and a common uncorrelated process with a given spectral index, while M3A replaces the common uncorrelated process with a common correlated process of the type ORF and a given spectral index. More technical details of each component of M2A or M3A are also included in this illustration.
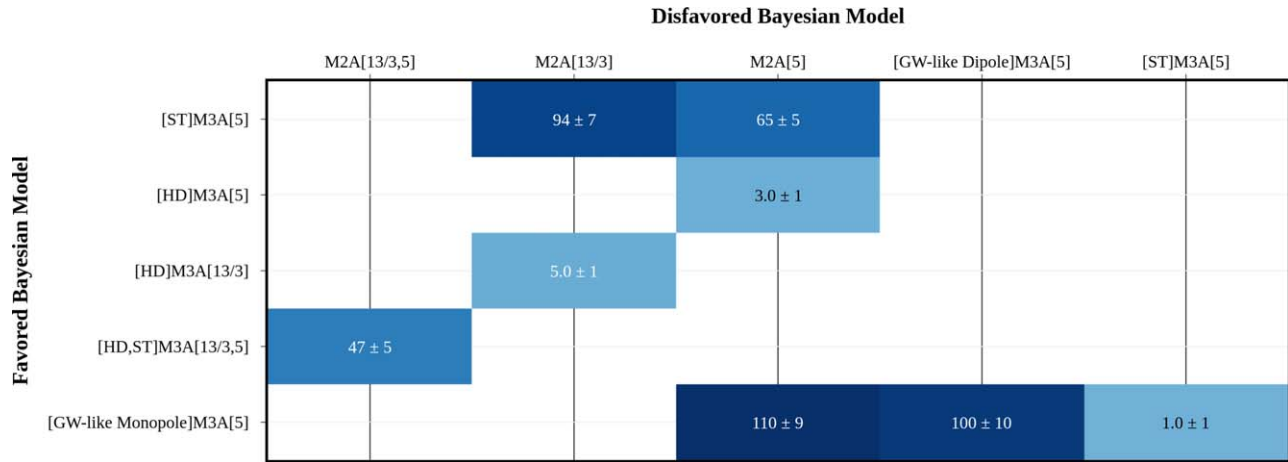
refers to an M3A model in which the type of correlation considered for the common process is HD (quadrupolar), and the spectral index of this common correlated process is fixed at 5. Some M3A models may include more than one type of common correlated red noise process. For these models, we include more than one type of ORF in the square bracket preceding the term "M3A." For instance, [HD,ST]M3A[13/3,5] means that the M3A contains two different correlated common signals, the first being a red noise process with a spectral index of 13/3 following HD-type correlations and the second being a red noise process with spectral index of 5 following ST-type correlations. Figure 8 shows a visual illustration of our terminology.

Extending the work presented in NG12.5, we show the results of 14 different Bayesian analyses that allow us to compare several models of interest. These models follow the structure outlined in Figure 8, and the resulting Bayes factors are presented in Figures 9 and 10 for the choices of ephemeris models DE438 and DE438 with BayesEphem corrections, respectively. Note that like NG12.5, for computational
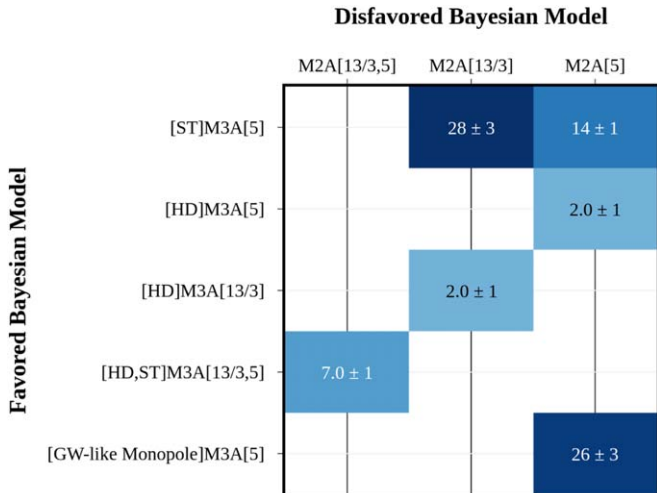
convenience, we have fixed all of the pulsar intrinsic white noise values for the analyses in this section.

As shown in Figure 9, the most favored Bayesian model is a GWB with GW-like monopolar correlations of Equation (25) with a Bayes factor greater than 100. Additionally, as a cross-check, we have reproduced the results of Chen et al. (2021a), where a model with ST correlations with a spectral index of 5, [ST]M3A[5], was compared to a model without correlations and a spectral index of 13/3, M2A[13/3]. We obtain a Bayes factor of about 94 in favor of [ST]M3A[5], which is consistent with their results.

We note, however, that the calculation of the [ST]M3A[5] to M2A[13/3] Bayes factor is not the right one to make to answer the question of whether or not the data prefer ST correlations to no correlations. If two models with different spectral indices and correlation types are compared, then the resulting Bayes factor simply indicates which Bayesian model, in its entirety, is preferred, not which correlation type is preferred by the data. In order to identify the preferred type of correlation, the spectral

Disfavored Bayesian Model

Favored Bayesian Model	M2A[13/3,5]	M2A[13/3]	M2A[5]	[GW-like Dipole]M3A[5]	[ST]M3A[5]
[ST]M3A[5]		94 ± 7	65 ± 5		
[HD]M3A[5]			3.0 ± 1		
[HD]M3A[13/3]		5.0 ± 1			
[HD,ST]M3A[13/3,5]	47 ± 5				
[GW-like Monopole]M3A[5]			110 ± 9	100 ± 10	1.0 ± 1

Figure 9. Table illustrating estimated Bayes factors from comparison of various Bayesian models. The choice of ephemeris model is fixed at DE438 for all of the comparisons in this figure. The darker the color of the blocks, the higher the value of the Bayes factor. The most favored model in all of the comparisons is a GW-like monopole. The naming convention of the models follows the structure defined in Figure 8. One can take advantage of the transitive nature of Bayes factors to compute Bayes factors for model comparisons that are not explicitly featured in this table. For instance, Bayes factors obtained from comparing [ST]M3A[5] to [HD]M3A[5] can be estimated by dividing the Bayes factor obtained from [ST]M3A[5] over M2A[5] by the Bayes factor obtained from [HD]M3A[5] over M2A[5]. The result is about $65/3 \approx 21$.

Disfavored Bayesian Model

Favored Bayesian Model	M2A[13/3,5]	M2A[13/3]	M2A[5]
[ST]M3A[5]		28 ± 3	14 ± 1
[HD]M3A[5]			2.0 ± 1
[HD]M3A[13/3]		2.0 ± 1	
[HD,ST]M3A[13/3,5]	7.0 ± 1		
[GW-like Monopole]M3A[5]			26 ± 3

Figure 10. Table illustrating estimated Bayes factors for comparison of various Bayesian models. In this table, the choice of ephemeris model is DE438 with the inclusion of BayesEphem corrections. The darker the color of the blocks, the higher the value of the Bayes factor. BayesEphem removes almost all of the significance from the ST and GW-like correlations. The naming convention of the models follows the structure defined in Figure 8.

index has to be fixed for the competing models. The difference in spectral indices between the two models could account for a significant fraction of the Bayes factor. Therefore, a more appropriate comparison is obtained by calculating the Bayes factor for [ST]M3A[5] versus M2A[5], where both models have the same spectral index. For this model comparison, we obtain a Bayes factor of about 65 in favor of [ST]M3A[5]. Though tantalizing, this Bayes factor is not sufficient to claim the detection of ST modes in the NANOGrav 12.5 yr data set.

There are several reasons for this. First, the Laplace approximation (see Romano & Cornish 2017) gives an S/N of about 2.9 for a Bayes factor of 65, which we do not deem sufficient for a detection claim. Furthermore, given the degeneracy between TT and ST modes when correlations are present but weak (see Figure 6 and the discussion in Section 3.1), an S/N ~ 2.9 in favor of ST correlations is not surprising, even when only TT modes are present in our data.

Additionally, accounting for uncertainties in the solar system ephemeris, we show that BayesEphem significantly reduces the Bayes factors to 14, as shown in Figure 10.[51] Finally, as we will show below (see Section 3.2.3), this result is very sensitive to the inclusion of one MSP, J0030+0451.

We note that the data slightly prefer the GW-like monopole to ST correlations; this is again unsurprising given the analyses of simulated data in Section 3.1, which show the ST and GW-monopole to be more or less interchangeable. Though these results are not compelling enough to claim a detection of any mode, they are sufficiently interesting to warrant follow-up analyses in future data sets currently under preparation.

Taking advantage of the transitive nature of Bayes factors, Figure 9 allows us to compute Bayes factors for model pairs that are not featured explicitly in Figure 9. For instance, Bayes factor obtained from comparing [ST]M3A[5] to [HD]M3A[5] can be estimated by dividing the Bayes factor obtained from [ST]M3A[5] over M2A[5] by the Bayes factor obtained from [HD]M3A[5] over M2A[5]. The result is about $65/3 \approx 21$.

Before we conclude this section, it is worth noting that not all models shown in Figure 9 are equally plausible from a theoretical standpoint. All metric theories of gravity must contain, at a minimum, the two Einsteinian +- and ×-modes. Thus, even though a model with only ST spatial correlations yields a high Bayes factor, ST GWs are not predicted on their own by any metric theory of gravity. On the other hand, a compound model such as [HD,ST]M3A[13/3,5] is more theoretically motivated. Additionally, the mixing ratio between the four different ORFs depends on the astrophysical source generating the GWs. In general, given a particular metric theory of gravity and sources of GWs, a linear combination of all/a subset of all polarization modes is expected.

3.2.2. Frequentist Analyses and S/N Estimation

As we discussed in Section 3.1, the noise-marginalized optimal statistic offers a very robust and computationally inexpensive alternative to the Bayesian techniques by

---

[51] See Vallisneri et al. (2020) and Aggarwal et al. (2019) for a discussion of how BayesEphem changes our sensitivity to the detection of Einsteinian GWs.

10
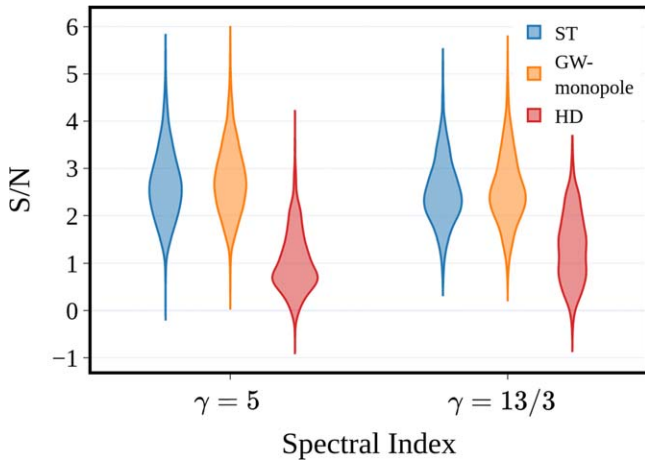
Figure 11. Violin plots depicting the S/N distribution of the 12.5 yr data set for ST (blue), HD (red), and GW-like monopole (orange) correlations at different spectral indices $\gamma = 5$ and $13/3$. The choice of the spectral index does not affect the S/N distribution of any of the correlation patterns. The ST and GW-like monopole yield similar S/Ns that are higher than the S/Ns obtained from HD correlations. This surprising result can be easily understood from the S/N evolution of SIM1 shown in Figure 6.

estimating the S/N. The S/N can be related to the Bayes factor using the Laplace approximation (Romano & Cornish 2017), specifically,

$$\ln B \approx \rho^2/2, \qquad (36)$$

where B is the Bayes factor and ρ is the S/N. The accuracy of the approximation improves as the likelihood function becomes more and more peaked relative to the joint prior probability distributions of the parameters (Romano & Cornish 2017). Later, we will show how our calculated Bayes factors are consistent with our S/N estimates through this Laplace relation.

Figure 11 shows the distribution of S/N for ST, GW-like monopole, and HD correlations obtained by calculating the noise-marginalized optimal statistic for the 12.5 yr data set. The S/N calculation is performed for two choices of the spectral index, 13/3 and 5. Even though the choice of spectral index does not significantly affect the results of the S/N estimation, the estimates for the amplitude of the red noise process change because of the covariance between amplitudes and spectral indices; the amplitude of a red noise process is lower, with a spectral index of 5 compared to a spectral index of 13/3. Figure 12 shows distributions of the amplitudes for spectral indices of 13/3 and 5. In the case of $\gamma = 5$, none of the correlated models match the amplitude of the common red noise process, suggesting that despite the high S/N value of the ST and GW-like monopole at this spectral index, these modes do not make up much of the observed common process. The best match occurs in the case of $\gamma = 13/3$, where the amplitude of a model with HD correlations overlaps somewhat significantly with the amplitude of the uncorrelated common red noise process. This is noted in NG12.5 as well.

3.2.3. MSP J0030+0451 and GW-monopole/ST Correlations

NG12.5 identified 10 of the 45 pulsars included in the analyses as the most significant contributors to the common red noise process that was detected. These pulsars are J1909−3744, J2317 +1439, J2043+1711, J1600−3053, J1918−0642, J1744−1134, J1910+1256, J0030+0451, J2145−0750, and J1640+2224. We performed our analyses anew, this time removing each of the above pulsars one at a time, and identified MSP J0030+0451 as

the main contributor to the GW-monopole/ST correlations. Removing this pulsar from our analyses results in the most significant changes to the S/N, recovered amplitude, and Bayes factor estimation. This effect can be seen in Figures 13 and 14 for the choice of spectral indices 13/3 and 5, respectively.

As shown in Figures 13 and 14, the optimal statistical analyses show that the S/N of the GW-like monopole (as well as ST) drops from about 2.8 to 2 when MSP J0030+0451 is removed. Simultaneously, the S/N of HD increases from 1 to about 2. Furthermore, the amplitude recovery for HD seems to be more consistent with the common red noise process, while the amplitudes of the GW-like monopole and ST become less consistent. Our Bayesian analyses agree with the optimal statistic results; when dropping MSP J0030+0451 from the analysis, the Bayes factor for [GW-like Monopole]M3A[5] to M2A[5] drops from about 100 to about 15, and the Bayes factor obtained for [HD]M3A[13/3] to M2A[13/3] increases from about 5 to about 10. It is worth pointing out that the changes in the optimal statistic and the Bayes factors are consistent with what we expect from the Laplace approximation.

We do not yet understand the details of how MSP J0030 +0451 is causing this effect, but we suspect incomplete noise modeling of this pulsar in our current analyses as the most plausible cause. Object J0030+0451 has been shown to be problematic in past analyses (see Hazboun et al. 2020b). This pulsar is close to the ecliptic, with its line of sight passing very close to the Sun, and this, in turn, produces a significant chromatic noise contribution in our data due to the solar wind. The appreciable solar wind contribution is specific to J0030 +0451; hence, we do not believe this affects our other pulsars significantly.

Object J0030+0451 requires special attention and is studied in depth as part of our advanced noise-modeling project, a flagship NANOGrav project that will be submitted for publication in the near future. Ongoing work shows that a more detailed noise model for J0030+0451 that includes a deterministic solar wind model, a dispersion measure (DM) Gaussian process, and a scattering component that models delays scaling like ν^{-4}, where ν is the radio frequency, greatly reduces the significance of the ST/GW-monopole signal. Such detailed noise models may need to be a part of future GW analyses.

3.3. Upper Limit Estimation

In the absence of a detection of any polarization mode of gravity, we place constraints on the amplitude of these modes using our Bayesian techniques for specific choices of spectral index and the number of expected polarization modes. As mentioned at the beginning of this section, upper limits are model-dependent. Different choices of priors, the number of polarization modes considered, and spectral indices can affect the results. We have chosen to report our 95% upper limits for eight different models. Details of the models are discussed below.[52]

---

[52] The results presented in this section are model-dependent. There are numerous theoretical models for how various non-Einsteinian polarization modes of gravity are generated; hence, there is no right choice for spectral index and amplitude prior ranges. We hope that interested readers will take the work presented in this section as a template and modify the model parameters as they see fit.
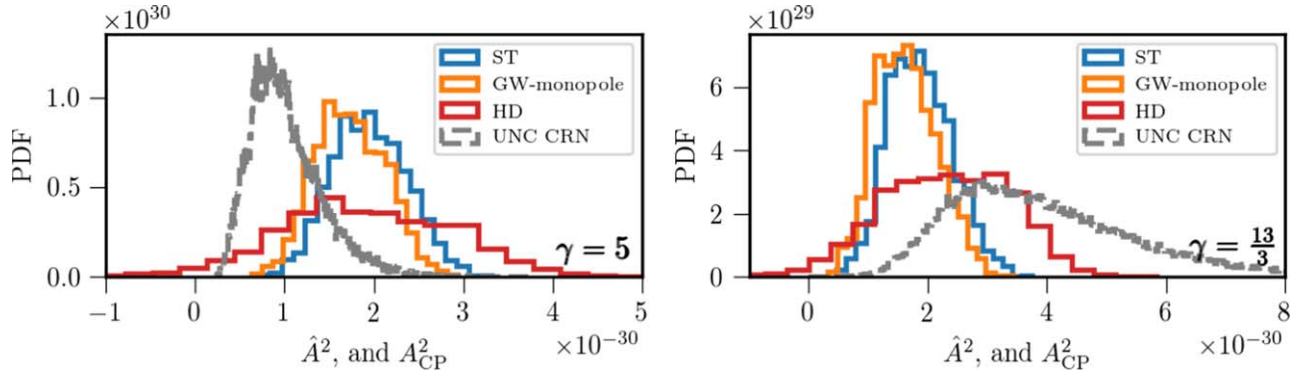
Figure 12. Distributions of the noise-marginalized optimal statistic for HD (red), GW-like monopole (orange), and ST (blue) spatial correlations for spectral indices of 5 (left panel) and 13/3 (right panel). The addition of the uncorrelated common process from a Bayesian search that only includes the autocorrelation terms, labeled "UNC CRN" (gray), guides us to determine which correlations make what portion of the observed common red noise process, regardless of the value of S/N. The correlations result in a range of amplitudes that are mostly not consistent with the amplitude of the common uncorrelated red noise process for a spectral index of 5, while the HD correlations' amplitude is somewhat more consistent with the UNC CRN for a spectral index of 13/3.
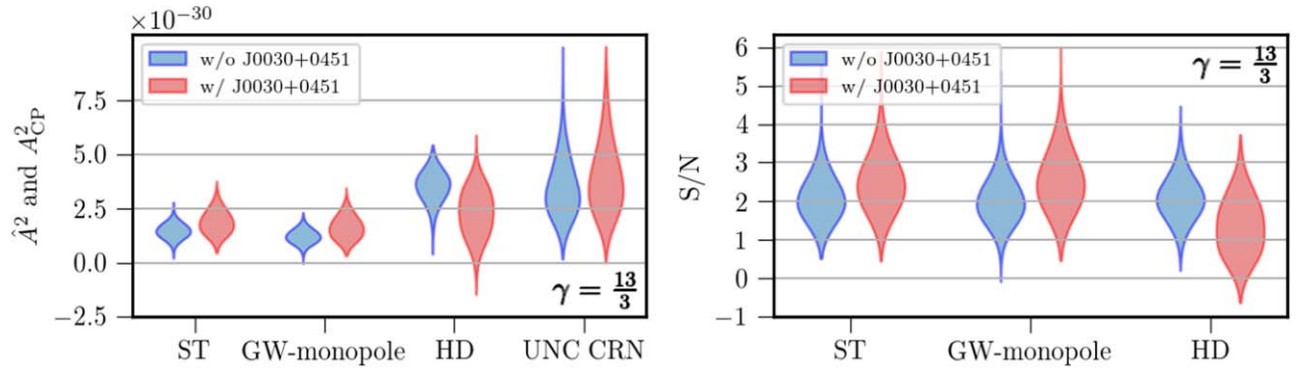
Figure 13. Distributions of the noise-marginalized optimal statistic and S/N for HD, GW-like monopole, and ST spatial correlations for $\gamma = 13/3$. The red violin plots show the results of optimal statistical analyses done on the full 12.5 yr data set, whereas the blue violin plots showcase the results of optimal statistical analyses done on the 12.5 yr data set excluding the pulsar J0030+0451. The S/N of the non-HD correlations is significantly reduced by omitting MSP J0030+0451. Additionally, there is a notable improvement in the consistency of the HD correlations' amplitude with the amplitude of the uncorrelated common red noise process (UNC CRN). Further improvements can also be seen in the form of an increase in the estimated HD S/N.
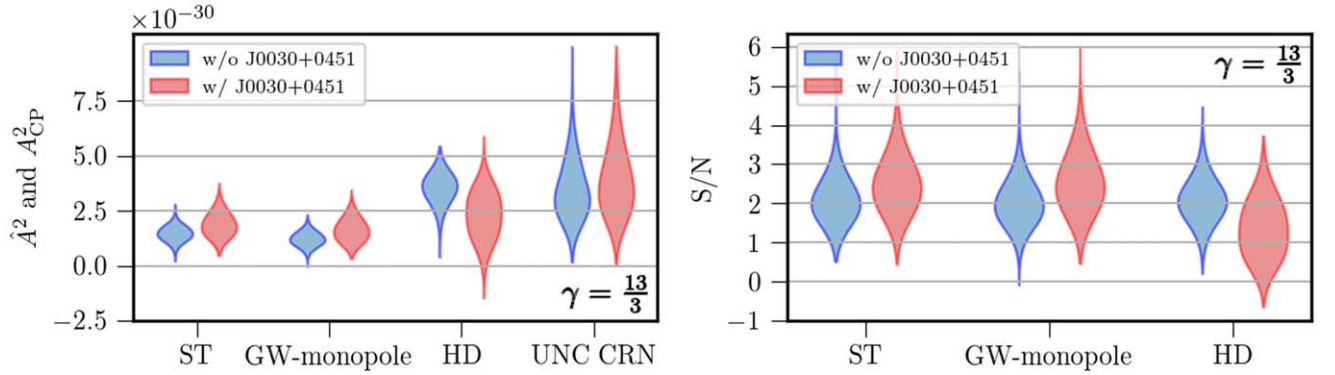
Figure 14. Distributions of the optimal statistic and S/N for HD, GW-like monopole, and ST spatial correlations for $\gamma = 5$. The red violin plots show the results of optimal statistical analyses done on the full 12.5 yr data set, whereas the blue violin plots showcase the results of optimal statistical analyses done on the 12.5 yr data set excluding the pulsar J0030+0451. The problem of the relatively high S/N of the non-HD correlations is resolved by omitting MSP J0030+0451. However, no noticeable improvement can be seen in the consistency of the amplitudes of any of the correlations relative to the amplitude of the uncorrelated common red noise process (UNC CRN).

Common red noise prior. All modes have uniform priors for their amplitude. More specifically,

$$A_{\mathrm{TT}} = \mathrm{Uniform}(10^{-18}, 10^{-12}), \quad (37)$$

$$A_{\mathrm{ST}} = \mathrm{Uniform}(10^{-18}, 10^{-12}), \quad (38)$$

$$A_{\mathrm{VL}} = \mathrm{Uniform}(10^{-18}, 10^{-15}), \quad (39)$$

$$A_{\mathrm{SL}} = \mathrm{Uniform}(10^{-18}, 10^{-16}). \quad (40)$$

	TT	ST	VL	SL
MG1111	$(1.1 \pm 0.06) \times 10^{-15}$	$(1.2 \pm 0.07) \times 10^{-15}$	$(2.2 \pm 0.1) \times 10^{-16}$	$(2.5 \pm 0.1) \times 10^{-17}$
MG1011	$(1.2 \pm 0.05) \times 10^{-15}$		$(2.6 \pm 0.09) \times 10^{-16}$	$(2.5 \pm 0.2) \times 10^{-17}$
MG1101	$(1.2 \pm 0.04) \times 10^{-15}$	$(1.1 \pm 0.05) \times 10^{-15}$		$(2.6 \pm 0.2) \times 10^{-17}$
MG1110	$(1.1 \pm 0.06) \times 10^{-15}$	$(1.1 \pm 0.05) \times 10^{-15}$	$(2.7 \pm 0.1) \times 10^{-16}$	
MG1001	$(1.3 \pm 0.05) \times 10^{-15}$			$(2.9 \pm 0.2) \times 10^{-17}$
MG1010	$(1.2 \pm 0.09) \times 10^{-15}$		$(2.7 \pm 0.1) \times 10^{-16}$	
MG1100	$(1.2 \pm 0.06) \times 10^{-15}$	$(1.2 \pm 0.07) \times 10^{-15}$		
MG1000	$(1.4 \pm 0.04) \times 10^{-15}$			

Figure 15. Heat map illustrating the 95% upper limit estimated for eight different models labeled based on the naming convention introduced in Section 3.3. The darker the color of a block, the higher the value of the upper limit. The spectral index for all of the polarization modes is fixed at $\gamma = 5$. The low value of the SL and VL upper limits attests to the high sensitivity of pulsar timing in detecting these modes.

We choose the above ranges so that for each of the modes, we are well below (for the lower bound on the priors) or well above (for the upper bound on the priors) the sensitivity range of our data. For the longitudinal modes (VL and SL), the upper limits on the priors are lower than for the transverse modes because pulsar timing experiments are more sensitive to those modes (especially the SL mode) than the transverse modes (TT and ST).

For the models in which the pulsar distances are needed (i.e., models with VL and SL modes), the distances follow a normal distribution. In cases where the pulsar distances are not well known, which constitutes the majority of our MSPs, we choose a mean and standard deviation of 1 and 0.2 kpc, respectively, for the normal distribution. Otherwise, if the pulsar distances are known more accurately, such as for MSP J1713+0747, we choose a more informed mean and standard deviation. In either case, we marginalize over the pulsar distances.

Naming convention. The naming convention adopted for the models considered in this subsection seeks to categorize all metric theories of gravity into eight families based on their predicted polarization content. The prefix "MG" is short for "metric theory of gravity," and the succeeding four digits speak to the existence, denoted by 1, or lack of existence, denoted by 0, of the possible four polarization modes TT, ST, VL, and SL.

For example, MG1000 is Einstein's general theory of relativity, and MG1100 is a theory with TT and ST modes (e.g., Brans–Dicke gravity). Note that all eight families of theories possess the TT mode, since this is required for all valid metric theories of gravity.

Spectral index. For convenience, we have taken the power in all modes to have a spectral index of $\gamma = 5$, which corresponds to a flat spectrum in Ω_{GW}, the ratio of the density in GWs to the critical density.

Intrinsic pulsar noise prior. All 45 pulsars in our analyses have log-uniform priors on the amplitude from -20 to -11. The choice of log-uniform priors on the intrinsic red noise is conservative, in the sense that it favors lower amplitudes for the intrinsic red noise relative to the common process (which has uniform priors), and results in larger upper limits on the common red noise process (see Hazboun et al. 2020a). The spectral indices of intrinsic pulsar red noises vary uniformly from zero to 7.

Spatial cross-correlations in the models. For computational convenience, we have not included correlations in most of our upper limit analyses. The minor improvements that are possible with the inclusion of cross-correlations do not justify the computational cost of performing such upper limit analyses. These improvements are particularly small in the case of the nontransverse polarization modes of gravity because the autocorrelation terms dominate the cross-terms significantly.

The upper limit values listed in Figure 15 can be used to place constraints on the detailed parameters of theories that couple to those modes, as well as the astrophysical sources that are capable of producing those modes. Such studies are outside the scope of this work.

We have also performed an additional analysis that includes both HD and ST correlations for the MG1100 model. Unlike the VL and SL modes, the magnitude of the cross-correlations for the TT and ST modes is of the same order as the autocorrelations. We therefore expect the inclusion of the cross-terms for theories with TT and ST modes to have the largest effect on their upper limits. The contour plot for the amplitude posterior of TT and ST in this model is shown in Figure 16. The upper limits obtained from this model ($A_{\mathrm{TT}}^{95\%} = (9.7 \pm 0.4) \times 10^{-16}$ and $A_{\mathrm{ST}}^{95\%} = (1.4 \pm 0.03) \times 10^{-15}$) are slightly smaller than the ones obtained from the MG1100 model without correlations (see Figure 15).

4. Summary

NANOGrav's 12.5 yr data set shows strong evidence for a common stochastic process, a red noise process with the same amplitude and spectral index across all pulsars. This common process, however, does not show strong evidence in favor of any GWB model with spatial correlations consistent with predictions of metric theories of gravity. The slight preferences for ST and GW-like monopolar correlations are not robust to the modeling of uncertainties in the solar system ephemeris and seem to be associated with one particular pulsar, J0030+0451. A thorough investigation of the J0030+0451 data set, along with improved and more sophisticated noise modeling for this and other pulsars, is likely to shed more light on this issue. Additionally, as our simulations show, given the baseline, the amplitude of the common process, and the levels of white and other noise present in the 12.5 yr data, it is possible to misconstrue a weak GWB with HD correlations as a GWB with ST or GW-like monopolar correlations.
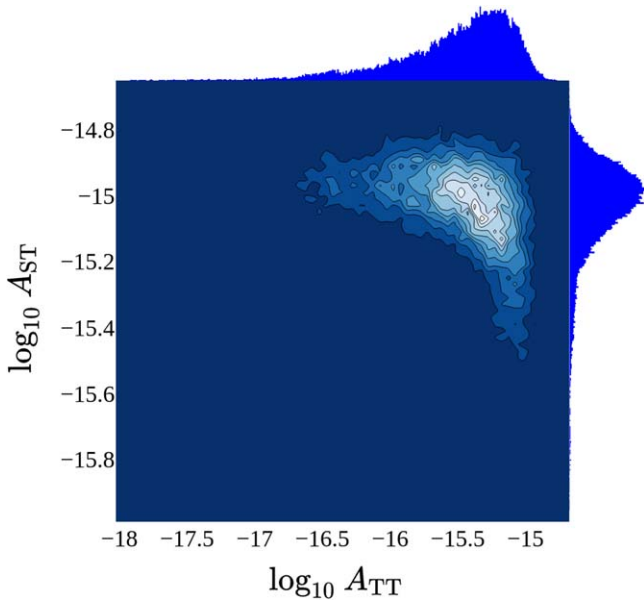
Figure 16. Two-dimensional contour plot illustrating the posterior distribution of ST and TT polarization modes obtained from a Bayesian model that contains both polarization modes as its correlated common process for a spectral index of $\gamma = 5$. The color scale for this contour plot is inverted; the darker a region is, the less likely it is for an amplitude to belong to that region. The amplitudes of both modes are centered around the same mean value.

Based on the work presented in this paper, we suggest the following as the minimum set of conditions required for a detection claim of alternative polarization modes of gravity using PTA data sets.

1. Bayes factors and S/N estimations must be consistent with the results of simulations. For instance, the simulations presented in this work suggest that it is possible to obtain S/Ns as high as 3 for the ST mode, even in the case of the absence of this mode in a PTA data set, so long as the TT mode is present. Hence, such S/N values are not sufficiently high for a detection claim of the ST mode in a PTA data set.

2. The amplitude of the uncorrelated common red noise signal should be consistent with the amplitude of the signal with a certain type of correlation to ensure that the process with correlations makes up much of the observed common process.

3. The results of detection analyses must be robust to the modeling of ephemeride uncertainties.

4. The results of detection analyses must be robust to the removal of individual pulsars. As mentioned, we found MSP J0030+0451 to be a significant contributor to the existence of the observed GW-like monopole (or ST correlations); removing this pulsar results in significant reduction of the S/N (from 2.8 to 2) and Bayes factor (from 100 to 10) in the case of a GW-like monopole.

In the absence of a detection, we place upper limits on the amplitudes of the various modes present in metric theories of gravity. Each of the models in this paper has its own set of upper limits that vary from model to model. For sources of GWs that can produce a GWB signal with a spectral index of 5, the estimated upper limits are reported in Figure 15. The reported upper limits can be used to place constraints on the parameters of theories that lead to such GW polarization content and the sources that are capable of producing GWs with various polarization modes. We do not attempt to make

such connections in this paper, but they should be useful in studies of alternative theories of gravity.

With the release of a new data set on the horizon, NANOGrav's 15 yr data set, we will continue to search for evidence of additional polarization modes of gravity. We anticipate that more pulsars, longer observation times, and improved noise modeling of pulsars will aid us greatly in finding and distinguishing the spatial correlation patterns in our data.

Appendix A
Dipole Radiation and PTA Signal

In order to construct a physically motivated model of a GWB in a PTA data set, Equation (34) needs be written in a more general form encapsulating the frequency-dependent effects of differing emission rates of binary sources of GWs. One such effect relevant to the study of alternative theories of gravity is caused by dipole radiation. To leading order in the post-Newtonian approximation and in ϑ (i.e., the difference in the self-gravitational binding energy per unit mass), the rate of change of the orbital energy of a binary source is (Will 1977)

$$\frac{dE}{dt} = \frac{2}{3} \lambda \mu \vartheta^2 \left(\frac{2\pi}{P}\right)^2 K(e) E, \qquad (A1)$$

where μ is the reduced mass, λ is the dipole parameter, P is the orbital period of the binary system, $K(e)$ is a function of the binary's eccentricity e, and E is system's instantaneous energy. Applying the Newtonian approximation, $E = -\frac{1}{2} M^{\frac{2}{3}} (2\pi f_s)^{\frac{2}{3}} \mu$, where M is the total mass and f_s is the orbital frequency, Equation (A1) can be used to calculate the rate of change of orbital frequency:

$$\frac{d \ln f_s}{dt} = 8\pi^3 \vartheta^2 \lambda K(e) \mu f_s^2. \qquad (A2)$$

Assuming a Keplerian rest frame, the instantaneous GW characteristic strain radiated by a circular binary system is (Sampson et al. 2015)

$$h_c(f) = 2(4\pi)^{\frac{1}{3}} \frac{f^{\frac{2}{3}} M^{\frac{5}{3}}}{D_L}, \qquad (A3)$$

where D_L is the luminosity distance to the source. This, alongside Equation (A2) and the fact that $f_s = f/2$, can be used to yield

$$h_c^D = C_D f^{-\frac{2}{3}}, \qquad (A4)$$

in which h_c^D is the characteristic amplitude of the GWB due to dipole radiation and C_D is a constant related to parameters introduced in Equation (A1) such that $\lambda = 0$ results in $C_D = 0$. Adding the quadrupolar contribution to the characteristic amplitude and treating it as more dominant than the
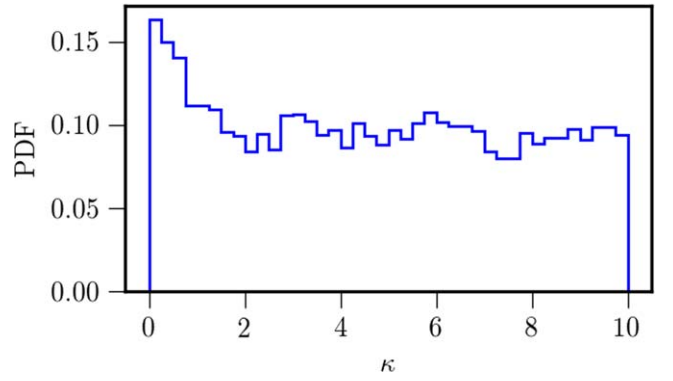
Figure 17. Bayesian posterior for the κ parameter obtained from NANOGrav's 12.5 yr data set using Equation (A5). We take γ_m to be 13/3 for the TT mode and γ_m to be 5 for the ST, VL, and SL modes, which is the appropriate choice for binary systems. We take log-uniform priors between -18 and -14 for the TT and ST modes, -18 and -15 for the VL mode, and -18 and -16 for the SL mode and a uniform prior between zero and 10 for the κ parameter (Cornish et al. 2018). The posterior curve is uninformative for large κ and shows a slight preference for small values. Based on this result, for all of the runs featured in this paper, the κ parameter is set to zero.

dipole contribution results in (Cornish et al. 2018)

$$S_{ab} = \left(\frac{1 + \kappa^2}{1 + \kappa^2 \left(\frac{f}{f_{yr}}\right)^{\frac{2}{3}}}\right) \sum_m \Gamma_{ab}^m A_m^2 \left(\frac{f}{f_{yr}}\right)^{3 - \gamma_m} \frac{1}{8\pi^2 f^3} \qquad (A5)$$

for a constant parameter κ denoting the relative value of the amplitude of dipole radiation over the amplitude of quadrupolar radiation driving the binary system to a merger.

In this paper, we have set λ, and consequently κ, to zero and use Equation (34) instead. This approximation follows from our analysis of the 12.5 yr data set using Equation (A5), with the choice of γ_m of 13/3 for the TT mode and γ_m of 5 for the ST, VL, and SL modes, which is appropriate for binary sources (Cornish et al. 2018). The result of such modeling is shown in Figure 17. The posterior for κ is uninformative for large values and shows a slight preference for values close to zero. Hence, for simplicity, we set the κ parameter to zero for all analyses in this paper.

Appendix B
Distinguishing Scalar–Tensor from GW-like Monopole Correlations in the Noise-marginalized Optimal Statistic

Separating ST from GW-like monopole correlations introduces new challenges to the usual detection procedure as outlined in Section 3.1. More explicitly, as can be seen in Figure 5, the S/Ns for the SIM2 and SIM3 data sets are overestimated (especially compared to the case for SIM1), and there are minor differences between the S/N values of the ST and GW-monopole correlations for all of the tested data sets.
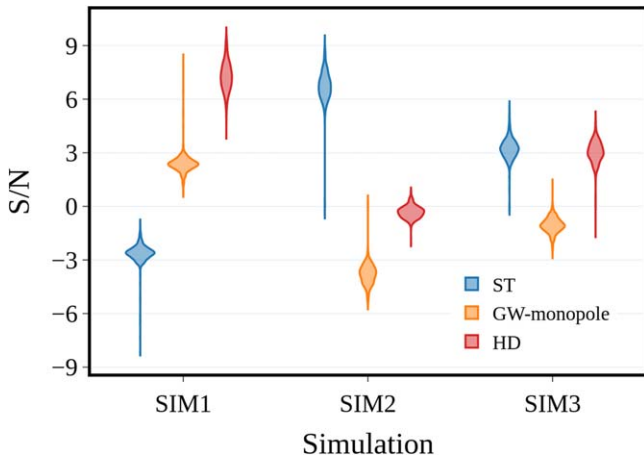
Figure 18. Violin plots showing the S/N distribution of the noise-marginalized optimal statistic for one realization of simulated data sets SIM1, SIM2, and SIM3 (see the main text for a description). The data are searched for three different correlation patterns simultaneously: ST (blue), HD (red), and GW-like monopole (orange). The S/N distribution for each simulated data set is obtained from the calculation of the noise-marginalized optimal statistic evaluated 1000 times. Significant improvements in the estimation of the S/N (compared to Figure 5) are made by changing the noise-marginalized optimal statistic to search for the ST, HD, and GW-like monopole simultaneously: (i) the S/N is no longer overestimated, and (ii) the overlap between the S/N values of the ST and GW-like monopole correlations is significantly reduced.

One way to mitigate these problems is to search for such modes simultaneously as opposed to separately, which has been the default procedure thus far for the noise-marginalized optimal statistic technique to compute S/N values. For instance, searching for ST and GW-like correlation patterns simultaneously in SIM2 results in reduction of the high S/N value of 17 to 7 for ST and 17 to −4 for the GW-like monopole (see Figure 18). The addition of this new feature to the noise-marginalized optimal statistic technique will be explored in depth in a separate paper.

Appendix C
Bayesian Methods

We used Markov Chain Monte Carlo (MCMC) methods to stochastically sample the joint posterior of our model parameter spaces and Monte Carlo integration to deduce marginalized distributions, where $\int f(\theta)p(\theta|d)d\theta \approx \langle f(\theta_i) \rangle$ for the integral of an arbitrary function $f(\theta)$ over the posterior $p(\theta|d)$ of which the samples $\{\theta_i\}$ are randomly drawn. Where necessary, we estimated the uncertainty on the marginalized posterior value to be the Monte Carlo sampling error of the location $\hat{\theta}_x$ of the xth quantile,

$$\frac{\sqrt{x(1-x)/N}}{p(\theta = \hat{\theta}_x|d)}, \quad (C1)$$

where N is the number of (quasi-)independent samples in our MCMC chain.

For the work presented in this paper, we employed the product-space method (Carlin & Chib 1995; Godsill 2001; Hee et al. 2015; Taylor et al. 2020) for model selection based on the relationship between the competing Bayesian models. This recasts model selection as a parameter estimation problem, introducing a model indexing variable that is sampled along

with the parameters of the competing models and controls which model likelihood is active at each MCMC iteration. The ratio of samples spent in each bin of the model indexing variable returns the posterior odds ratio between models. The efficiency of model transitions is controlled by our prior model probabilities, which we usually set to be equal; there are two ways to control the model jumping in the Bayesian analysis. One could change the prior to not be uniform, or one can weight the likelihood so that a model that is less favored is visited by the MCMC more often. The former is more difficult to deconvolve. In the second case, the odds ratio can then be calculated by unweighting the model parameter before calculating the true odds ratio. However, one can improve the odds ratio computation by performing a pilot run, whose odds ratio estimate can be used to reweight the models in a follow-up run. This will ensure more equitable chain visitation to each model, after which the model index posterior is reweighted back to the true model contrast.

Appendix D
Software

We used the software packages `enterprise` (Ellis et al. 2020) and `enterprise_extensions` (Taylor et al. 2021) to perform the Bayesian and frequentist searches. The software required to perform the analyses discussed in this paper is available in the master branch of `enterprise` and `enterprise_extensions`. These packages implement the signal models, likelihood, and priors. We used the software package `PTMCMCSampler` (Ellis & van Haasteren 2017) to perform the MCMC for the Bayesian searches.

ORCID iDs

Paul T. Baker ⓘ https://orcid.org/0000-0003-2745-753X
Harsha Blumer ⓘ https://orcid.org/0000-0003-4046-884X
Paul R. Brook ⓘ https://orcid.org/0000-0003-3053-6538
Sarah Burke-Spolaor ⓘ https://orcid.org/0000-0003-4052-7838
Maria Charisi ⓘ https://orcid.org/0000-0003-3579-2522
Shami Chatterjee ⓘ https://orcid.org/0000-0002-2878-1502
James M. Cordes ⓘ https://orcid.org/0000-0002-4049-1882
Neil J. Cornish ⓘ https://orcid.org/0000-0002-7435-0869
Fronefield Crawford ⓘ https://orcid.org/0000-0002-2578-0360
H. Thankful Cromartie ⓘ https://orcid.org/0000-0002-6039-692X
Megan E. DeCesar ⓘ https://orcid.org/0000-0002-2185-1790
Paul B. Demorest ⓘ https://orcid.org/0000-0002-6664-965X
Timothy Dolch ⓘ https://orcid.org/0000-0001-8885-6388
Elizabeth C. Ferrara ⓘ https://orcid.org/0000-0001-7828-7708
William Fiore ⓘ https://orcid.org/0000-0001-5645-5336
Emmanuel Fonseca ⓘ https://orcid.org/0000-0001-8384-5049
Peter A. Gentile ⓘ https://orcid.org/0000-0001-8158-683X
Deborah C. Good ⓘ https://orcid.org/0000-0003-1884-348X
Jeffrey S. Hazboun ⓘ https://orcid.org/0000-0003-2742-3321
Ross J. Jennings ⓘ https://orcid.org/0000-0003-1082-2342
Megan L. Jones ⓘ https://orcid.org/0000-0001-6607-3710
David L. Kaplan ⓘ https://orcid.org/0000-0001-6295-2881
Luke Zoltan Kelley ⓘ https://orcid.org/0000-0002-6625-6450
Joey Shapiro Key ⓘ https://orcid.org/0000-0003-0123-7600
Nima Laal ⓘ https://orcid.org/0000-0002-9197-7604
Duncan R. Lorimer ⓘ https://orcid.org/0000-0003-1301-966X
Tingting Liu ⓘ https://orcid.org/0000-0001-5766-4287
Jing Luo ⓘ https://orcid.org/0000-0001-5373-5914
Alexander McEwen ⓘ https://orcid.org/0000-0001-5481-7559

Maura A. McLaughlin ⓘ https://orcid.org/0000-0001-7697-7422
Cherry Ng ⓘ https://orcid.org/0000-0002-3616-5160
David J. Nice ⓘ https://orcid.org/0000-0002-6709-2566
Timothy T. Pennucci ⓘ https://orcid.org/0000-0001-5465-2889
Scott M. Ransom ⓘ https://orcid.org/0000-0001-5799-9714
Paul S. Ray ⓘ https://orcid.org/0000-0002-5297-5278
Brent J. Shapiro-Albert ⓘ https://orcid.org/0000-0002-7283-1124
Joseph Simon ⓘ https://orcid.org/0000-0003-1407-6607
Ingrid H. Stairs ⓘ https://orcid.org/0000-0001-9784-8670
Daniel R. Stinebring ⓘ https://orcid.org/0000-0002-1797-3277
Kevin Stovall ⓘ https://orcid.org/0000-0002-7261-594X
Joseph K. Swiggum ⓘ https://orcid.org/0000-0002-1075-3837
Jacob E. Turner ⓘ https://orcid.org/0000-0002-2451-7288
Michele Vallisneri ⓘ https://orcid.org/0000-0002-4162-0033
Sarah J. Vigeland ⓘ https://orcid.org/0000-0003-4700-9072
Haley M. Wahl ⓘ https://orcid.org/0000-0001-9678-0299
Caitlin A. Witt ⓘ https://orcid.org/0000-0002-6020-9274

References

Abbott, B. P., Abbott, R., Abbott, T. D., et al. 2016a, PhRvX, 6, 041015
Abbott, B. P., Abbott, R., Abbott, T. D., et al. 2016b, PhRvL, 116, 221101
Abbott, B. P., Abbott, R., Abbott, T. D., et al. 2017a, PhRvL, 118, 221101
Abbott, B. P., Abbott, R., Abbott, T. D., et al. 2017b, ApJ, 848, L13
Abbott, B. P., Abbott, R., Abbott, T. D., et al. 2018a, PhRvL, 120, 201102
Abbott, B. P., Abbott, R., Abbott, T. D., et al. 2018b, PhRvL, 120, 031104
Abbott, B. P., Abbott, R., Abbott, T. D., et al. 2019a, PhRvL, 123, 011102
Abbott, B. P., Abbott, R., Abbott, T. D., et al. 2019b, PhRvD, 100, 104036
Abbott, R., Abbott, T. D., Abraham, S., et al. 2020a, PhRvD, 102, 043015
Abbott, R., Abbott, T. D., Abraham, S., et al. 2020b, ApJ, 896, L44
Abbott, R., Abbott, T. D., Abraham, S., et al. 2020c, ApJ, 900, L13
Abbott, R., Abbott, T. D., Abraham, S., et al. 2021a, PhRvD, 104, 022004
Abbott, R., Abbott, T. D., Abraham, S., et al. 2021b, PhRvD, 103, 122002
Addazi, A., Cai, Y.-F., Gan, Q., Marciano, A., & Zeng, K. 2021, SCPMA, 64, 290411
Aggarwal, K., Arzoumanian, Z., Baker, P. T., et al. 2019, ApJ, 880, 116
Alam, M. F., Arzoumanian, Z., Baker, P. T., et al. 2021, ApJS, 252, 4
Allen, B. 1988, PhRvD, 37, 2078
Anholm, M., Ballmer, S., Creighton, J. D. E., Price, L. R., & Siemens, X. 2009, PhRvD, 79, 084030
Arzoumanian, Z., Baker, P. T., Blumer, H., et al. 2020, ApJL, 905, L34
Arzoumanian, Z., Baker, P. T., Blumer, H., et al. 2021, arXiv:2104.13930
Arzoumanian, Z., Baker, P. T., Brazier, A., et al. 2018, ApJ, 859, 47
Arzoumanian, Z., Brazier, A., Burke-Spolaor, S., et al. 2016, ApJ, 821, 13
Ashoorioon, A., Rostami, A., & Firouzjaee, J. T. 2021, PhRvD, 103, 123512
Bailes, M., Barr, E., Bhat, N. D. R., et al. 2016, in MeerTime - the MeerKAT Key Science Program on Pulsar Timing, Proc.of MeerKAT Science: On the Pathway to the SKA (Trieste: SISSA), 11
Bécsy, B., & Cornish, N. J. 2021, CQGra, 38, 095012
Berezinsky, V., Hnatyk, B., & Vilenkin, A. 2004, BaltA, 13, 289
Blanco-Pillado, J. J., Olum, K. D., & Siemens, X. 2018, PhLB, 778, 392
Blanco-Pillado, J. J., Olum, K. D., & Wachter, J. M. 2021, PhRvD, 103, 103512
Bonetti, M., Sesana, A., Barausse, E., & Haardt, F. 2018, MNRAS, 477, 2599
Borah, D., Dasgupta, A., & Kang, S. K. 2021, PhRvD, 104, 063501
Brandenburg, A., Clarke, E., He, Y., & Kahniashvili, T. 2021, PhRvD, 104, 043513
Caprini, C., Durrer, R., & Siemens, X. 2010, PhRvD, 82, 063511
Carlin, B. P., & Chib, S. 1995, J R Stat B, 57, 473
Chakrabortty, J., Lazarides, G., Maji, R., & Shafi, Q. 2021, JHEP, 2021, 114
Chamberlin, S. J., & Siemens, X. 2012, PhRvD, 85, 082001
Chang, C.-F., & Cui, Y. 2021, arXiv:2106.09746
Chen, Z.-C., Wu, Y.-M., & Huang, Q.-G. 2021b, arXiv:2109.00296
Chen, Z.-C., Yuan, C., & Huang, Q.-G. 2021a, SCPMA, 64, 120412
Chiang, C.-W., & Lu, B.-Q. 2021, JCAP, 2021, 049
Cordes, J. M., & Jenet, F. A. 2012, ApJ, 752, 54
Cornish, N. J., O'Beirne, L., Taylor, S. R., & Yunes, N. 2018, PhRvL, 120, 181101
Damour, T., & Vilenkin, A. 2000, PhRvL, 85, 3761
Damour, T., & Vilenkin, A. 2001, PhRvD, 64, 064008
Damour, T., & Vilenkin, A. 2005, PhRvD, 71, 063510
Demorest, P. B., Ferdman, R. D., Gonzalez, M. E., et al. 2013, ApJ, 762, 94

Desvignes, G., Caballero, R. N., Lentati, L., et al. 2016, MNRAS, 458, 3341
Detweiler, S. 1979, ApJ, 234, 1100
Di Bari, P., Marfatia, D., & Zhou, Y.-L. 2021, JHEP, 2021, 193
Dvorkin, I., & Barausse, E. 2017, MNRAS, 470, 4547
Eardley, D. M., Lee, D. L., & Lightman, A. P. 1973, PhRvD, 8, 3308
Eardley, D. M., Lee, D. L., Lightman, A. P., Wagoner, R. V., & Will, C. M. 1973c, PhRvL, 30, 884
Ellis, J., & Lewicki, M. 2021, PhRvL, 126, 041304
Ellis, J., & van Haasteren, R. 2017, Jellis18/PTMCMCSampler: Official Release, doi:10.5281/zenodo.1037579
Ellis, J. A., Vallisneri, M., Taylor, S. R., & Baker, P. T. 2020, ENTERPRISE: Enhanced Numerical Toolbox Enabling a Robust PulsaR Inference SuitE, Zenodo, doi:10.5281/zenodo.4059815
Ellis, J. A., Vallisneri, M., Taylor, S. R., & Baker, P. T. 2020, ENTERPRISE: Enhanced Numerical Toolbox Enabling a Robust PulsaR Inference SuitE, v3.0.0, Zenodo, doi:10.5281/zenodo.4059815
Enoki, M., Inoue, K. T., Nagashima, M., & Sugiyama, N. 2004, ApJ, 615, 19
Gair, J. R., Romano, J. D., & Taylor, S. R. 2015, PhRvD, 92, 102003
Ghayour, B., Khodagholizadeh, J., Afkani, M., Torkamani, M. R., & Vahedi, A. 2021, IJMPD, 30, 2150023
Godsill, S. J. 2001, J Comput Graph Stat, 10, 230
Goncharov, B., Shannon, R. M., Reardon, D. J., et al. 2021, ApJL, 917, L19
Gorghetto, M., Hardy, E., & Nicolaescu, H. 2021, JCAP, 2021, 034
Hazboun, J. S., Simon, J., Siemens, X., & Romano, J. D. 2020a, ApJL, 905, L6
Hazboun, J. S., Simon, J., Taylor, S. R., et al. 2020b, ApJ, 890, 108
Hee, S., Handley, W. J., Hobson, M. P., & Lasenby, A. N. 2015, MNRAS, 455, 2461
Hellings, R. W., & Downs, G. S. 1983, ApJL, 265, L39
Hobbs, G., & Edwards, R. 2012, Tempo2: Pulsar Timing Package, Astrophysics Source Code Library, ascl:1210.015
Hunter, J. D. 2007, CSE, 9, 90
Inc, P. T. 2015, Collaborative data science, Montreal, QC: Plotly Technologies Inc, https://plot.ly
Islo, K., Simon, J., Burke-Spolaor, S., & Siemens, X. 2019, arXiv:1906.11936
Jaffe, A. H., & Backer, D. C. 2003, ApJ, 583, 616
Joshi, B. C., Arumugasamy, P., Bagchi, M., et al. 2018, JApA, 39, 51
Kelley, L. Z., Blecha, L., & Hernquist, L. 2016, MNRAS, 464, 3131
Kelley, L. Z., Blecha, L., Hernquist, L., Sesana, A., & Taylor, S. R. 2017, MNRAS, 471, 4508
Kelley, L. Z., Blecha, L., Hernquist, L., Sesana, A., & Taylor, S. R. 2018, MNRAS, 477, 964
Kerr, M., Reardon, D. J., Hobbs, G., et al. 2020, PASA, 37, e020
Lazarides, G., Maji, R., & Shafi, Q. 2021, PhRvD, 104, 095004
Lee, K. J. 2016, in ASP Conf. Ser. 502, Frontiers in Radio Astronomy and FAST Early Sciences Symposium 2015, ed. L. Qain & D. Li (San Francisco, CA: ASP), 19
Lee, K. J., Jenet, F. A., & Price, R. H. 2008, ApJ, 685, 1304
Lentati, L., Taylor, S. R., Mingarelli, C. M. F., et al. 2015, MNRAS, 453, 2576
Li, H.-H., Ye, G., & Piao, Y.-S. 2021, PhLB, 816, 136211
Lin, C.-M. 2021, JCAP, 2021, 056
Lommen, A. N., & Backer, D. C. 2001, ApJ, 562, 297
Madison, D. R., Chernoff, D. F., & Cordes, J. M. 2017, PhRvD, 96, 123016
McWilliams, S. T., Ostriker, J. P., & Pretorius, F. 2012, arXiv:1211.4590
Mingarelli, C. M. F., Grover, K., Sidery, T., Smith, R. J. E., & Vecchio, A. 2012, PhRvL, 109, 081104
Mingarelli, C. M. F., Lazio, T. J. W., Sesana, A., et al. 2017, NatAs, 1, 886
Nakai, Y., Suzuki, M., Takahashi, F., & Yamada, M. 2021, PhLB, 816, 136238
Neronov, A., Pol, A. R., Caprini, C., & Semikoz, D. 2021, PhRvD, 103, L041302
Newman, E., & Penrose, R. 1962, JMP, 3, 566
Ng, C. 2017, in IAU Symp. 337, Pulsar Astrophysics the Next Fifty Years, ed. P. Weltevrede et al. (Dordrecht: Reidel), 179
O'Beirne, L., Cornish, N. J., Vigeland, S. J., & Taylor, S. R. 2019, PhRvD, 99, 124039
Ölmez, S., Mandic, V., & Siemens, X. 2010, PhRvD, 81, 104028
Perera, B. B. P., DeCesar, M. E., Demorest, P. B., et al. 2019, MNRAS, 490, 4666
Pol, N. S., Taylor, S. R., Kelley, L. Z., et al. 2021, ApJL, 911, L34
Poletti, D. 2021, JCAP, 2021, 052
Qin, W., Boddy, K. K., & Kamionkowski, M. 2021, PhRvD, 103, 024045
Ransom, S., Brazier, A., Chatterjee, S., et al. 2019, BAAS, 51, 195
Ravi, V., Wyithe, J. S. B., Hobbs, G., et al. 2012, ApJ, 761, 84
Ravi, V., Wyithe, J. S. B., Shannon, R. M., & Hobbs, G. 2015, MNRAS, 447, 2772
Roedig, C., & Sesana, A. 2012, JPhCS, 363, 012035
Romano, J. D., & Cornish, N. J. 2017, LRR, 20, 2

Rosado, P. A., Sesana, A., & Gair, J. 2015, MNRAS, 451, 2417
Ryu, T., Perna, R., Haiman, Z., Ostriker, J. P., & Stone, N. C. 2018, MNRAS, 473, 3410
Sampson, L., Cornish, N. J., & McWilliams, S. T. 2015, PhRvD, 91, 084055
Sanidas, S. A., Battye, R. A., & Stappers, B. W. 2013, ApJ, 764, 108
Sazhin, M. V. 1978, SvA, 22, 36
Schutz, K., & Ma, C.-P. 2016, MNRAS, 459, 1737
Sesana, A. 2013, MNRAS, 433, L1
Sesana, A., Shankar, F., Bernardi, M., & Sheth, R. K. 2016, MNRAS, 463, L6
Sesana, A., & Vecchio, A. 2010, PhRvD, 81, 104008
Sesana, A., Vecchio, A., & Colacino, C. N. 2008, MNRAS, 390, 192
Sesana, A., Vecchio, A., & Volonteri, M. 2009, MNRAS, 394, 2255
Shannon, R. M., Ravi, V., Coles, W. A., et al. 2013, Sci, 342, 334
Shannon, R. M., Ravi, V., Lentati, L. T., et al. 2015, Sci, 349, 1522
Sharma, R. 2021, arXiv:2102.09358
Siemens, X., Creighton, J., Maor, I., et al. 2006, PhRvD, 73, 105001
Siemens, X., Ellis, J., Jenet, F., & Romano, J. D. 2013, CQGra, 30, 224015
Siemens, X., Mandic, V., & Creighton, J. 2007, PhRvL, 98, 111101
Starobinskiǐ, A. A. 1979, JETPL, 30, 682
Taylor, S. R., Baker, P. T., Hazboun, J. S., Simon, J. J., & Vigeland, S. J. 2021, Enterprise Extensions v2.3.3 https://github.com/nanograv/enterprise_extensions

Taylor, S. R., Vallisneri, M., Ellis, J. A., et al. 2016, ApJL, 819, L6
Taylor, S. R., van Haasteren, R., & Sesana, A. 2020, PhRvD, 102, 084039
Vagnozzi, S. 2021, MNRAS, 502, L11
Vallisneri, M. 2020, libstempo: Python wrapper for Tempo2, Astrophysics Source Code Library. ascl:2002.017
Vallisneri, M., Taylor, S. R., Simon, J., et al. 2020, ApJ, 893, 112
van Haasteren, R., & Levin, Y. 2010, MNRAS, 401, 2372
van Haasteren, R., Levin, Y., Janssen, G. H., et al. 2011, MNRAS, 414, 3117
Verbiest, J. P. W., Lentati, L., Hobbs, G., et al. 2016, MNRAS, 458, 1267
Vigeland, S. J., Islo, K., Taylor, S. R., & Ellis, J. A. 2018, PhRvD, 98, 044003
Volonteri, M., Haardt, F., & Madau, P. 2003, ApJ, 582, 559
Will, C. M. 1977, ApJ, 214, 826
Will, C. M. 1993, Theory and Experiment in Gravitational Physics (Cambridge: Cambridge Univ. Press)
Witten, E. 1984, PhRvD, 30, 272
Wu, L., Gong, Y., & Li, T. 2021a, arXiv:2105.07694
Wu, Y.-M., Chen, Z.-C., & Huang, Q.-G. 2021b, arXiv:2108.10518
Wyithe, J. S. B., & Loeb, A. 2003, ApJ, 590, 691
Yi, Z., & Zhu, Z.-H. 2021, arXiv:2105.01943
Yunes, N., & Siemens, X. 2013, LRR, 16, 9